Supporting Online Material (SOM)

Material and Methods

Bacterial strains, plasmids and culture conditions

The bacterial strains and plasmids used in this study are listed in Table S4. All *V. cholerae* and *E. coli* strains were grown aerobically, at 30°C and 37°C, respectively. Unless otherwise noted, growth medium consisted of Luria Bertani (LB) medium (1% Tryptone, 0.5% Yeast Extract, 0.5% NaCl, pH 7.5). LB-agar and LB-soft agar contained 1.5% (wt/vol) and 0.3% (wt/vol) granulated agar (Difco), respectively. Concentrations of antibiotics used, where appropriate, were as follows: ampicillin (100 μg/ml), rifampicin (100 μg/ml), kanamycin (50 μg/ml), and chloramphenicol (5 μg/ml).

Recombinant DNA techniques

DNA manipulations were carried out using standard molecular techniques. VpsT point mutants were generated using QuikChange site-directed mutagenesis kit (Stratagene), following the manufacturer's instructions. In-frame deletions and *vpsLp-lacZ* single-copy chromosomal reporter strains were generated as described previously (*S1-3*). Point mutations and chromosomal deletions/insertions were sequence-verified.

Protein expression and purification

The coding region corresponding to full-length VpsT from *V. cholerae* O1 El Tor (VCA0952) (*S4*) was amplified by standard PCR and cloned into a modified pET28a expression plasmid (Novagen) yielding N-terminally hexahistidine-tagged SUMO fusion proteins. The hexahistidine-tagged SUMO-moiety was cleavable using the protease Ulp-1 from *S. cerevisiae*.

Native and selenomethionine-derivatized proteins were overexpressed in *E. coli* T7 Express or T7 Crystal Express cells, respectively (NEB). For the expression of native proteins, cells were grown in Terrific Broth (TB) media supplemented with 50 μg/ml kanamycin at 37°C. At a cell optical density corresponding to an absorbance of 0.8-1.0 at 600 nm (OD_{600}), the temperature was reduced to 18°C, and protein production was induced with 1 mM IPTG. Selenomethionine-derivatized proteins were produced in cells grown in M9 minimal media supplemented with 50 μg/ml kanamycin, 1 μg/ml thiamine, 1 μg/ml biotin, 0.4% glucose and 40 μg/ml of each of the 20 amino acids with selenomethionine substituting for methionine. Protein expression was induced at OD_{600} of 0.4-0.5. After 16 hours, cells were harvested by centrifugation, resuspended in NiNTA buffer A (25 mM Tris-Cl, pH 7.5, 550 mM NaCl and 20 mM imidazole), and flash-frozen in liquid nitrogen.

After cell lysis by sonication and removal of cell debris by centrifugation, clear lysates were loaded onto NiNTA columns (HisTrap; GE Healthcare) equilibrated in NiNTA buffer A. The resin was washed with 20 column volumes of NiNTA buffer A, and proteins were eluted in a single step of NiNTA buffer A supplemented with 500 mM imidazole. Proteins were buffer exchanged into desalting buffer (25 mM Tris-HCl, pH

7.5, 550 mM NaCl, 10mM imidazole, 5mM β-mercaptoethanol), and affinity tags were removed by incubation with the yeast protease Ulp-1 at 4°C overnight. Cleaved proteins were collected in the flow-through during NiNTA affinity chromatography, and were subjected to size exclusion chromatography on a Superdex 200 column (GE Healthcare) equilibrated in gel filtration buffer (25 mM Tris-HCl, pH 7.5, 550 mM NaCl, 2mM DTT). Proteins were concentrated on a Centricon ultrafiltration device (10 kDa cutoff; Millipore) to a final concentration of approximately 1-4 mM. Protein aliquots were flash frozen in liquid nitrogen and stored at -80°C.

Crystallization, data collection and structure determination

Crystals were obtained by hanging drop vapor diffusion by mixing equal volumes of protein (10-40 mg/ml) and reservoir solution followed by incubation at 20°C. For crystallization of the c-di-GMP bound state, protein incubated with c-di-GMP was subjected to size exclusion chromatography for removal of unbound nucleotide prior to crystallization. The reservoir solution contained 0.1 M Tris-HCl pH 7.0, 0.8 M Potassium sodium tartrate tetrahydrate, 3-5% Polyethylene glycol monomethyl ether 5,000, and 8-12% xylitol. Crystals appeared within 3-10 days with typical dimensions of 0.40 mm x 0.08 mm x 0.08 mm. For cryo-protection, crystals were soaked in reservoir solution supplemented with 25% xylitol. Cryo-preserved crystals were flash-frozen and stored in liquid nitrogen. Data was collected on frozen crystals at 100 K using synchrotron radiation at the National Synchrotron Light Source (NSLS, Brookhaven National Laboratory, beamline X29).

Data reduction was carried out with the software package XDS (*S5*). Experimental phases were obtained from multi-wavelength anomalous diffraction (MAD) experiments on crystals grown from selenomethionine-derivatized proteins. By using the software package HKL2MAP/Shelx (*S6*), 28 out of 32 heavy atom positions could be determined. Solvent flattening was carried out by using the program ShelxE (*S6*). The structure of c-di-GMP-bound VpsT was determined by molecular replacement using the software package PHENIX (*S7*) with the apo-structure as the search model. Refinement in PHENIX (*S7*) and COOT (*S8*) yielded the final models. Data collection and refinement statistics are summarized in Table S1. Illustrations were made in Pymol (DeLano Scientific).

Large-Scale Enzymatic production of c-di-GMP

Large amounts of c-di-GMP were synthesized enzymatically using a highly active mutant of the diguanylate cyclase WspR and GTP as a substrate (*S9*). High purity of the compound was achieved by preparative reverse-phase HPLC followed by lyophilization. In a final step of the product analysis, it was enzymatically tested as a substrate for phosphodiesterases. Cyclic di-GMP concentration was determined based on absorbance at 254 nm in comparison with commercially obtained standard of known concentration (Biolog Life Science Institute).

Size-exclusion chromatography (SEC)-coupled static multi-angle light scattering

For SEC-coupled multi-angle light scattering, purified protein (~10 μg/μl or 400 μM, injected concentration) was subjected to SEC using a Shodex KW-803 column (JM

Science, Inc.) equilibrated overnight in gel filtration buffer (25 mM Tris-HCl pH 7.5, 400-600 mM NaCl, and 2 mM DTT). Where specified, wild-type or mutant VpsT was incubated with excess c-di-GMP for 30 minutes at room temperature prior to injection. In additional sets of experiments, c-di-GMP was also added to the gel filtration buffer at a concentration of 40 μM. The chromatography system was coupled to a 3-angle light scattering detector (miniDAWN TREOS) and a refractive index detector (Optilab rEX) (Wyatt Technology). Data were collected every second at a flow rate of 0.5 ml/min. Data analysis was carried out using the program ASTRA, yielding the molar mass and mass distribution (polydispersity) of the sample. For normalization of the light scattering detectors and data quality control, monomeric bovine serum albumin (BSA; Sigma) was used.

Reverse-phase HPLC

SEC eluted protein peaks from above were collected, concentrated to a final concentration of 10 μg/μl, heat denatured at 95°, and centrifuged at 14,000 rpm for 10 minutes. Resulting supernatants were filtered through Microcon Centrifugal Filter Units (Millipore, 10 kDa cut-off) and separated on a C18 reverse-phase column using a methanol-phosphate gradient (buffer A: 100 mM potassium phosphate monobasic, pH 6.0; buffer B: 30% methanol/70% buffer A). Protein bound c-di-GMP was identified by comparison to a nucleotide standard.

Analytical ultracentrifugation

Sedimentation velocity experiments were carried out using an XL-I analytical ultracentrifuge (Beckman Coulter) equipped with an AN-60 Ti rotor. Proteins (8 and 12 μM) were diluted in buffer (25 mM Tris-HCl pH 7.5, 550 mM NaCl, 2 mM DTT) in the absence or presence of c-di-GMP (25 μM), and were analyzed at a centrifugation speed of 130,000 x g. Data collection was carried out at 280 nm, followed by data analysis using the program SedFit (version 11.0).

Isothermal titration calorimetry

Apparent dissociation constants (K_d) and stoichiometry of interactions were measured by isothermal titration calorimetry (ITC) using a VP calorimeter (Microcal, Amherst, MA). Calorimetric titrations of c-di-GMP (250 μM in the syringe; 10 μl injections) and wild-type or mutant VpsT (25 μM in the cuvette) were carried out at 20°C in assay buffer (25 mM Tris-HCl pH 7.5, 550 mM NaCl, 2mM DTT) with a spacing of 180 or 300 sec between injections. ITC data were analyzed by integrating heat effects normalized to the amount of injected protein and curve-fitting based on a single-site binding model using the Origin software package (Microcal). The dissociation constant was derived from the data by using standard procedures.

RNA isolation

V. cholerae cells were grown aerobically overnight in LB in the absence of arabinose. Cultures were diluted 1:500 in fresh media with the inducer arabinose (0.1%) and grown aerobically at 30°C with shaking at 200 rpm to an OD_{600} of 0.3 to 0.4. Two ml

aliquots of cultures were collected by centrifugation for 2 min at room temperature. Cell pellets were immediately resuspended in 1 ml Trizol reagent (Invitrogen) and stored at -80°C. Total RNA was isolated from the cell pellets according to the manufacturer's instructions (Invitrogen). Contaminating DNA was removed by incubating RNA with RNase-free DNase I (Ambion), and an RNeasy Mini kit (Qiagen) was used to clean up RNA after DNase digestion.

Quantitative PCR (qPCR)

qPCR was performed as described previously (*S3*). Briefly, cDNA was synthesized from 1 μg of RNA from each sample using an iScript cDNA Synthesis Kit (Bio-Rad). The product was used as a template in a subsequent PCR reaction using Expand High Fidelity PCR System (Roche). PCR reaction conditions were as follows: 94°C for 2 min, then 25 cycles of 94°C for 30 sec, 55°C for 30 sec and 72°C for 30 sec, and a final 72°C for 2 min. Amplified products were analyzed on a 1.5% agarose gel and quantified using ImageQuant software (Molecular Dynamics). Intensities of each DNA band were normalized to the corresponding gyrA band. Three biological replicates were conducted for each treatment tested and reactions lacking reverse transcriptase were used as negative controls.

Electromobility shift assays

Electromobility shift assays (EMSAs) were performed using purified wild-type or mutant VpsT proteins and DNA fragments tiling the *vpsL* promoter region. Briefly, biotinylated primers were used to amplify the corresponding chromosomal regions by

standard PCR using genomic DNA as a template. Commercially available 60 bp-duplex biotin end-labeled Epstein-Barr Nuclear Antigen (EBNA) DNA (Pierce) was used as a negative control. Binding reactions contained final concentrations of 5 nM labeled DNA, 1 μM protein, and 0.05 μg/μl Poly-dI-dC in the binding buffer (10 mM Tris-HCl pH 7.5, 50 mM KCl, 75 mM NaCl, 10 mM $MgCl_2$, 5% xylitol, 1 mM DTT, 0.1 mM EDTA). Where specified, c-di-GMP was added to a final concentration of 50 μM. After 40 min incubation at room temperature, DNA was resolved in 5% TBE-polyacrylamide gels (BioRad) with 0.5X TBE as running buffer (45 mM Tris Base, 45 mM Boric Acid, 1 mM EDTA). DNA mobility was visualized using LightShift Chemiluminescent EMSA kit (Pierce) following the manufacturer's instructions.

β-Galactosidase assays

V. cholerae cells were grown aerobically overnight in LB in the absence of arabinose. Cultures were diluted 1:500 in fresh media with the inducer arabinose (0.1%) and grown aerobically at 30°C with shaking at 200 rpm to an OD_{600} of 0.3 to 0.4. β-galactosidase assays were carried out in MultiScreen 96-well microtiter plates fitted onto a MultiScreen filtration system (Millipore) using a previously published procedure (*S10*). The assays were repeated with two biological replicates and at least six technical replicates.

Gene expression profiling

Microarrays used in this study were performed as described previously (*S3*), except reference RNA was obtained from a Δ*vpsT V. cholerae* strain (Fy_Vc_4435)

harboring pBAD/*myc*-His-B grown to mid-exponential phase (OD_{600} of 0.3 to 0.4) in LB with the inducer arabinose (0.1%), inoculated (1:500 dilution) with overnight grown culture. Differentially regulated genes were determined using three biological replicates and two technical replicates for each treatment (6 data points for each spot) with the SAM software (*S11*) using 2-fold differences in gene expression and 3% false discovery rate (FDR) as cut-off values. Microarray data has been deposited in the NCBI Gene Expression Omnibus (GEO) database.

Spot morphology and motility assay

Analysis of spot morphologies of strains carrying plasmids with either wild-type VpsT or VpsT point mutants ($VpsT^{M17D}$, $VpsT^{R134A}$, or $VpsT^{I141E}$) were carried out by spotting 2 μl of 1:200-diluted overnight cultures onto LB agar plates supplemented with 100 μg/ml ampicillin and 0.02% arabinose. Spot cultures were incubated for 1 day at 30°C and photographed. Spot morphologies shown are representation of two independent biological replicates. Motility assays were carried out with LB-soft agar (0.3% agar) inoculated from a single colony grown overnight on LB agar at 30°C. After incubation for 18 to 20 h at 30°C, the migration zone diameter was measured and compared between strains.

Detailed Results and Discussion

Additional structural analysis

VpsT is a 25.8 kDa, conserved protein in *Vibrio* with sequence similarity to CsgD, FixJ and other LuxR family transcriptional regulators. Full-length VpsT from *V. cholerae* was purified to homogeneity by using standard liquid chromatography (see Material and Methods for details). Crystallization trials carried out with VpsT in the absence or presence of c-di-GMP yielded isomorphous crystals with similar unit cell dimensions, space group and diffraction properties (Table S1).

For the nucleotide-free protein, crystals grown with selenomethionine-substituted protein diffracted X-rays to a maximal resolution of 3.1 Å. Data sets were collected at 3 wavelengths: the selenium anomalous scattering peak wavelength, the inflection, and a remote wavelength. The structure was solved by multi-wavelength anomalous dispersion (MAD) phasing, determining the position of 28 out of 32 selenium atoms. VpsT crystallized in the space group $P4_12_12$ with 4 molecules in the asymmetric unit (Fig. S9). The polypeptide chain of protomers A, B and C could be traced and built with high confidence into the experimentally phased maps. The REC domain of molecule D was also well resolved. The HTH domain of molecule D was largely disordered, and only the position of two of the 4 helices could be determined.

Cyclic di-GMP-bound VpsT diffracted X-rays to a resolution of 2.8 Å. The structure was solved by molecular replacement using a protomer of the nucleotide-free structure as the search model. Four protomers could be located in the asymmetric unit with similar properties described above for apo-VpsT. The electron density maps

revealed extra density at the base of the A-B and C-D dimer interfaces that was reminiscent of two stacked c-di-GMP molecules (Fig. 1C and S9A). A similar conformation of the nucleotide has been observed at the inhibitory site of diguanylate cyclases such as PleD and WspR, and in crystals of the nucleotide (*S9, S12-14*). Within a VpsT dimer, the two-fold symmetric c-di-GMP dimer stabilizes a two-fold symmetric protein assembly, using a similar binding mode as has been observed in other c-di-GMP-protein complexes that involves π-stacking interactions in addition to hydrogen bonds between the guanidinium groups of the binding site's arginine residues and the central guanine bases of c-di-GMP (*S9, S12*).

The asymmetric unit and crystal packing of the c-di-GMP-bound state is shown in Fig. S9A. In both, the nucleotide-free and c-di-GMP-bound crystals, the dimers A-B and C-D are formed via isologous contacts. The two equivalent, two-fold symmetric dimers (A-B and C-D) pack via a surface at the base of protomer A and C with an interfacial area of 519 $Å^2$. Energetic calculations yield a positive value for the free energy gain for the interaction mediated by this interface, suggesting that it is not biologically relevant. There are no interactions between the REC domains of protomers A and B with protomer D, and between the REC domains of protomers B and C. Crystal packing interactions involving the HTH domains were not considered since they would interfere with DNA binding.

Since the overall crystal packing contacts were preserved in the nucleotide-bound structure, it suggests that c-di-GMP stabilizes one of the dimers that can form under certain conditions such as in the crystallization drop. In the c-di-GMP-bound structure, there are minor adjustments of the packing, especially with regard to the c-di-GMP-

mediated dimerization interface, but the protomers move as rigid bodies (Fig. S9B and S9C). Superposition of protomers indicates a rigid conformation of VpsT with regard to the relative orientation of the REC and HTH domains (rmsd between 0.5 and 0.9 Å over all atoms) independent of c-di-GMP binding, with a buried surface area between the domains of 1355 $Å^2$, suggesting that such a conformation is unlikely to be due to crystal packing forces (Fig. S9B).

The c-di-GMP-stabilized dimer discussed here consists of protomers A and B, while the nucleotide-independent dimer is formed by protomer A and a protomer B from an adjacent asymmetric unit. Equivalent interactions occur in the crystals between molecules C and D, and their symmetry mates. These interactions between protomers are propagated throughout the crystal lattice, suggesting that VpsT can form higher-order oligomers with two polymerization sites per dimer (Fig. S9A).

The c-di-GMP-bridged protein interface has hydrophobic character and is largely stabilized by nucleotide binding to the base of α6 (Fig. 1C and S3B). An isoleucine residue at the center of the interface, located in α6, was mutated to glutamate in this study as a way to destabilize the formation of this dimer. A similar dimer involving α6 has been observed in the structure of a LuxR family two-component response regulator from *Aurantimonas sp. SI85-9A1* (PDB code 3cz5; Malashkevich et al.; unpublished) (Fig. S10A). In this case, phosphate and magnesium coordinating residues, as well as residues involved in the conformational switching, are similar to the response regulators PhoB and WspR suggesting that this REC domain is under control by phosphorylation (Fig. S10B). A bound phosphate ion at the putative phosphorylation site observed in the crystal structure supports this hypothesis. This response regulator lacks the VpsT c-di-

GMP binding motif, but the structural resemblance and crystal packing contacts suggest a common mode for dimerization in this class of LuxR family response regulators, some of which appear to be regulated by ligand binding rather than phosphorylation.

The constitutive, c-di-GMP-independent dimer interface contains polar interactions in addition to a hydrophobic groove at the bottom, a pocket accommodating the methionine residue crucial for formation of this dimer (M^{17}; Fig. S3A). In addition, the putative phosphorylation site (D^{60}; Fig. S3A) is part of this interface, which may explain why expression of $VpsT^{M17D}$, $VpsT^{D60A}$ or $VpsT^{D60E}$ in a Δ*vpsT* strain affects motility and spot morphology in a similar manner (Fig. S7). While mutations in the putative phosphorylation site were designed to mimic a constitutively inactive ($VpsT^{D60A}$) or a constitutively active ($VpsT^{D60E}$) state, they had indistinguishable activities in gene expression and motility assays, suggesting that phosphorylation does not play a major role in the regulation of VpsT.

Comparing the REC domain of VpsT to canonical REC domain-containing proteins such as PhoB, which are regulated by phosphorylation, suggests that VpsT employs a distinct mechanism (Fig. S10B). Many important residues for phospho-induced switching in other REC domains are not conserved in VpsT. While the phopshorylation site and one of the magnesium-coordinating aspartates are present in VpsT (D^{60} and D^{14}, respectively), it contains a serine-substitution in the position of the second magnesium-coordinating residue (S^{13}) (Fig. S11). The lysine residue that usually forms a salt bridge with the phosphate moiety in canonical REC domains is replaced with an aspartate residue (D^{112}). Only one of the switch residues is conserved (F^{109}), whereas the crucial threonine residue in PhoB (or serine in some other REC proteins) is a cysteine

in VpsT (C^{90}). The switch residue F^{109} is involved in the conserved network of residues, and is engaged in a hydrophobic packing contact with the tryptophan residue of the c-di-GMP binding motif, possibly suggesting an allosteric path connecting the two dimer interfaces similar to that of canonical REC domains (Fig. S11B) (*S15*).

While the dimer interfaces are predominantly hydrophobic, the DNA binding site is largely polar. To model the protein-DNA interaction we used an alignment with the HTH•DNA complex structure of NarL (PDB entry 1zg5) (*S16*), a response regulator, which shares 38% identity and a total of 85% sequence similarity with VpsT in its DNA-binding motif. Out of 24 residues participating in the formation of the protein-DNA interface in the NarL crystal structure (*S17*), 11 are identical and 10 show conserved or semi-conserved substitutions in VpsT. Most of these residues lie in helix α10, buried in the large groove of DNA, while the rest are interspersed in helices α8, α9, and α11, as well as in the connecting loop regions. Furthermore, all ten residues participating in direct hydrogen bond contacts with the DNA phosphate backbone or bases are conserved, with seven of them being identical between the two proteins. Substitutions were observed in two of the three residues forming hydrogen bonds with nucleobases in both VpsT and CsgD, presumably conferring specificity to the recognized DNA sequence (NarL-T^{183} is a serine in VpsT and CsgD; NarL-K^{192} is a histidine in VpsT and a tyrosine in CsgD). Thus, while consensus DNA motifs for NarL and CsgD binding have been proposed (*S18-20*), VpsT recognition sites remain to be experimentally determined.

Based on this analysis, helix α10 was identified as a structural motif that binds to the major groove of DNA (Fig. S12). Considering the c-di-GMP-independent VpsT dimer, superpositioning of the HTH domains with a HTH•DNA complex structure of the

homolog NarL suggests a binding mode in which the DNA is bent in a 90°-angle, similar to that of transcriptional regulators such as the catabolite activator protein (*S16, S21*) (Fig. S12A). In contrast, the DNA molecules in the c-di-GMP-mediated VpsT dimer model run anti-parallel to each other, a configuration that would introduce DNA loops (Fig. S12B). DNA looping has been described as a mode of action for λ repressor and as a mechanism for the regulation of the *lac*, *gal* and *ara* operons (*S22, S23*). Notably, while AraC binds multiple operator sites to stabilize DNA loops, the catabolite activator protein participates in the regulatory network of the *ara* operon, presumably by bending the DNA (*S24*). Based on its structure, VpsT would have the capacity to introduce both types of DNA deformations, bending and looping.

Given that the distribution of VpsT binding sites on the *Vibrio* chromosomes remains unknown, we cannot rule out the possibility that both the c-di-GMP dependent and independent interfaces could serve a regulatory function on DNA, introducing distinct deformation upon binding. In DNA mobility shift studies, stronger binding to three of the four *vpsL* promoter fragments was observed with $VpsT^{M17D}$, the mutant that cannot form the c-di-GMP-independent dimer, compared to wild-type VpsT (Fig. 2A). Although the c-di-GMP-independent dimer appears to affect DNA binding negatively for this particular promoter, its competence for DNA binding would depend on the distribution of VpsT recognition sequences across the *V. cholerae* genome. In addition to bending and looping DNA by dimeric VpsT, it would be feasible that VpsT forms higher order complexes on DNA upon c-di-GMP binding. A plausible tetramer, based on the VpsT crystal structure, would involve the c-di-GMP-mediated dimerization of VpsT

dimers (Fig. S12C). Alternatively, two c-di-GMP-stabilized dimers could interact via the nucleotide independent interface.

Oligomerization of VpsT in solution

The dimeric, intercalated c-di-GMP conformation observed in the VpsT crystal structure has been also shown as prevalent under similar solution conditions (*S25*), and is hence unlikely to be due to crystal packing artifacts. Moreover, isothermal titration calorimetry (ITC) experiments revealed an apparent affinity for c-di-GMP (~3 μM) with a 1:1 binding stoichiometry and large unfavorable change in enthropy (ΔS ~ -34 kcal/mole). Consistent with potential cooperativity between nucleotide binding and VpsT dimerization through the corresponding interface, mutations destabilizing either interaction abolished c-di-GMP recognition ($VpsT^{R134A}$, $VpsT^{W131F}$, $VpsT^{T133V}$ and $VpsT^{I141E}$, respectively; Fig. S4). Conversely, VpsT carrying a disruptive mutation in the alternative dimerization interface, $VpsT^{M17D}$, bound c-di-GMP with similar to wild-type thermodynamic parameters (Fig. S4; Table S2).

Elution of the nucleotide-free, wild-type VpsT showed a concentration-dependent shift in the protein peak during analytical size exclusion chromatography (Fig. S5, box), indicating conversion between different oligomeric species. In addition, incubation with c-di-GMP caused the protein to fall out of solution unless the salt concentration was raised (up to 600 mM NaCl depending on protein concentration) or xylitol (5-10%) was present. Salt-stabilized, c-di-GMP-bound protein eluted in a yet distinct fractionation volume, consistent with oligomerization through both crystallographic interfaces. Analysis of wild-type VpsT by analytical ultracentrifugation corroborated c-di-GMP-

dependent oligomerization, with trimers being observed at higher concentration (Fig. S6). A further increase in protein concentration increased the heterogeneity of the sample and the tendency for protein aggregation.

In order to observe the differential effect of the two interfaces on c-di-GMP-dependent regulation of VpsT in solution, we resorted to SEC-coupled static multi-angle light scattering (MALS), a technique that reports the absolute molecular weight of macromolecules in any elution volume and independent of their shape (Fig. S5; Table S2). Experiments were conducted in high-salt buffer conditions (400-600mM NaCl) and at relatively high protein concentrations (~10 μg/μl or 400μM, injected concentration) in order to minimize c-di-GMP-driven polymerization and maximize association differences (see Fig. S5, box). While VpsT^{M17D} in the absence of c-di-GMP existed exclusively as a monomer, wild-type VpsT, VpsT^{R134A}, and VpsT^{I141E} exhibited molecular weights that were intermediate between those of a monomer and a dimer with relative concentration dependence throughout the elution peak. As reported for other systems (*S26*), such behavior is likely due to rapidly interchanging oligomeric species, with the constitutive, c-di-GMP-independent interface mediating sufficient dimerization on the SEC column. Cyclic di-GMP-mediated shifts to higher molecular weights were observed for VpsT^{M17D} and wild-type VpsT, confirming a role for the second, c-di-GMP-dependent interface in signal-induced VpsT oligomerization. Shifts were more pronounced when c-di-GMP was included in the SEC buffer, compared to samples that were pre-incubated with c-di-GMP but analyzed in a mobile phase lacking the nucleotide (Fig. S5B-D, right column). As expected, mutants incapable of nucleotide recognition, VpsT^{R134A} and VpsT^{I141E}, showed no change in oligomerization state in the presence or absence of the nucleotide.

Taken together, our solution data indicates a role for c-di-GMP in introducing a novel interaction interface in the VpsT quaternary structure. It is important to note that while cellular salt and protein concentrations might be significantly lower than the ones used in our *in vitro* studies, VpsT oligomerization *in vivo* would be facilitated by additional factors such as DNA binding, the architecture of available VpsT binding sequences on the *Vibrio* genome, and/or association with putative interacting partners among others.

Detailed analysis of the gene expression profiles

Whole genome expression profiling comparison of a Δ*vpsT* strain harboring wild-type VpsT or VpsT point mutants ($VpsT^{M17D}$, $VpsT^{D60A}$, $VpsT^{R134A}$ or $VpsT^{I141E}$) to that of cells harboring the pBAD vector allowed us to gain an insight into the complementation capacity of each clone. The overexpression levels were determined to be moderate, about 1.5-fold above the expression of vpsT in the rugose strain, according to qPCR (Fig. S13).

Expression of wild-type *vpsT* led to the differential regulation of 54 genes (≥2-fold change in expression, 3% FDR): 31 induced and 23 repressed, respectively. A complete list of differentially regulated genes is provided in Table S3. Besides genes involved in biofilm matrix production, which are discussed in the main text, transcription of a set of genes, predicted to be in a three gene operon (VC1583: *sodC*, encoding superoxide dismutase, 1.7-fold change; VC1585: *katB*, encoding catalase; VC1584: *ankB*, protein of unknown function), is increased in the Δ*vpsT* strain harboring wild-type

VpsT. This observation suggests that enhanced oxidative stress resistance in rugose variants and cells grown in biofilms are likely to be controlled in part by VpsT.

VpsT with a mutation in either c-di-GMP binding ($VpsT^{R134A}$, $VpsT^{W131F}$, $VpsT^{R133V}$ or $VpsT^{M17D/R134A}$) or the c-di-GMP-dependent dimerization interface ($VpsT^{I141E}$) was unable to complement phenotypes associated with lack of *vpsT* (Fig. 2 and 3; Fig. S8). In contrast, a VpsT version unable to undergo c-di-GMP-independent dimerization ($VpsT^{M17D}$) was able to complement and even over-complement such phenotypes (Fig. 2). Expression the $VpsT^{M17D}$ led to the differential expression of 84 genes (≥2-fold change in expression, 3% FDR): 45 induced and 39 repressed, respectively. A complete list of regulated genes is provided in Table S3. For instance, expression of genes in the *vps*-I cluster were 2-fold greater in a Δ*vpsT* strain harboring $VpsT^{M17D}$ relative to that harboring wild-type VpsT. Similarly, expression of greater number of flagellar biogenesis genes was downregulated in the $VpsT^{M17D}$-expressing Δ*vpsT* strain relative to that harboring wild-type VpsT. This result was confirmed by using a qPCR for transcript levels of *flaA*, one of the genes showing significant repression in the microarrays (Fig. S7A and B). Transcription of *vpsR*, *cdgA* (VCA0074), VCA0075, *vpvA* and *vpvB*, genes whose products positively regulate biofilm matrix production, were also higher in a Δ*vpsT* strain harboring $VpsT^{M17D}$. Taken together, our results suggest that c-di-GMP-independent dimerization of VpsT could prevent DNA binding or contribute to the fine-tuning of the transcriptional response.

Comparison with VpsT homologs and CsgD

Vibrio parahaemolyticus, the causative agent of the most common *Vibrio*-associated, seafood-borne gastroenteritis, utilizes VpsT and VpsR homologs to regulate capsular polysaccharide (Cps) production and biofilm formation (*S27*). However, the function of these proteins in Cps production differs significantly from their counterparts in *V. cholerae*. For example, the VpsR homolog CpsR is not required for basal levels of *cps* expression but appears to induce *cps* gene expression in strains predicted to have elevated levels of c-di-GMP (*S28, S29*), which may indicate a similar, c-di-GMP-dependent regulation as has been described for FleQ (*S30*), a distant homolog of VpsR/CpsR in *P. aeruginosa*. The VpsT homolog in *Vibrio parahaemolyticus*, CpsS, negatively regulates *cps* transcription as *cpsS* deletion resulted in increased Cps production and super-rugose colony formation. Although the mechanisms by which CpsR and CpsS regulate *cps* transcription are yet to be determined, the presence of a VpsT-like c-di-GMP binding motif (W[F/L/M][T/S]R) in CpsS suggests that c-di-GMP may regulate CpsS function.

As mentioned before, VpsT is homologous to the transcriptional regulator CsgD from *E. coli* and *Salmonella enterica serovar Typhimurium*. CsgD is required for the production of the two major extracellular matrix components, exopolysaccharides and proteinaceous fimbriae (curli), leading to the development of a unique colony morphology characterized by extensive corrugation and biofilm formation (*S31*). As a consequence, *E. coli* and *S. enterica* mutants lacking CsgD produce flat and smooth colonies, similarly to *V.cholerae* mutants lacking VpsT (*S32, S33*).

CsgD and VpsT share an overall similar architecture harboring a C-terminal LuxR type HTH domain and an N-terminal REC domain with homology to FixJ/LuxR family response regulators of two-component signal transduction systems. Similar to VpsT, the REC domain of CsgD contains the conserved aspartate residue (D^{59} in CsgD) predicted to be phosphorylated, but lacks crucial residues necessary for phosphotransfer. The mechanism by which CsgD gets activated is yet unknown. As discussed in the main text, the c-di-GMP binding motif is not conserved in CsgD, but other small molecules may bind to its receiver domain to regulate CsgD activity (*S34*).

References

S1. J. C. Fong, K. Karplus, G. K. Schoolnik, F. H. Yildiz, *J. Bacteriol.* **188**, 1049 (2006).

S2. B. Lim, S. Beyhan, J. Meir, F. H. Yildiz, *Mol. Microbiol.* **60**, 331 (2006).

S3. N. J. Shikuma, F. H. Yildiz, *J. Bacteriol.* **191**, 4082 (2009).

S4. C. Casper-Lindley, F. H. Yildiz, *J. Bacteriol.* **186**, 1574 (2004).

S5. W. Kabsch, *Journal of Applied Crystallography* **26**, 795 (1993).

S6. G. M. Sheldrick, *Acta Crystallogr. A* **64**, 112 (2008).

S7. P. D. Adams *et al.*, *Acta Crystallogr. D* **58**, 1948 (2002).

S8. P. Emsley, K. Cowtan, *Acta Crystallogr. D* **60**, 2126 (2004).

S9. N. De *et al.*, *PLoS Biol.* **6**, e67 (2008).

S10. N. J. Shikuma *et al.*, *J. Bacteriol.* **191**, 5147 (2009).

S11. V. G. Tusher, R. Tibshirani, G. Chu, *Proc. Natl. Acad. Sci. U.S.A.* **98**, 5116 (2001).

S12. C. Chan *et al.*, *Proc. Natl. Acad. Sci. U.S.A.* **101**, 17084 (2004).

S13. M. Egli *et al.*, *Proc. Natl. Acad. Sci. U.S.A.* **87**, 3235 (1990).

S14. Y. C. Liaw *et al.*, *FEBS Lett.* **264**, 223 (1990).

S15. R. Gao, A. M. Stock, *Annu. Rev. Microbiol.* **63**, 133 (2009).

S16. A. E. Maris *et al.*, *Biochemistry* **44**, 14538 (2005).

S17. E. Krissinel, K. Henrick, *J. Mol. Biol.* **372**, 774 (2007).

S18. E. Brombacher, C. Dorel, A. J. Zehnder, P. Landini, *Microbiology* **149**, 2847 (2003).

S19. K. L. Tyson, A. I. Bell, J. A. Cole, S. J. Busby, *Mol. Microbiol.* **7**, 151 (1993).

S20. I. Baikalov *et al.*, *Biochemistry* **35**, 11053 (1996).

S21. S. C. Schultz, G. C. Shields, T. A. Steitz, *Science* **253**, 1001 (1991).

S22. K. S. Matthews, *Microbiol. Rev.* **56**, 123 (1992).

S23. R. Schleif, *Annu. Rev. Biochem.* **61**, 199 (1992).

S24. R. B. Lobell, R. F. Schleif, *J. Mol. Biol.* **218**, 45 (1991).

S25. Z. Zhang, S. Kim, B. L. Gaffney, R. A. Jones, *J. Am. Chem. Soc.* **128**, 7015 (2006).

S26. B. D. Zoltowski, B. R. Crane, *Biochemistry* **47**, 7012 (2008).

S27. Z. T. Guvener, L. L. McCarter, *J. Bacteriol.* **185**, 5431 (2003).

S28. R. B. Ferreira, L. C. Antunes, E. P. Greenberg, L. L. McCarter, *J. Bacteriol.* **190**, 851 (2008).

S29. Y. K. Kim, L. L. McCarter, *J. Bacteriol.* **189**, 4094 (2007).

S30. J. W. Hickman, C. S. Harwood, *Mol. Microbiol.* **69**, 376 (2008).

S31. U. Romling, *Cell. Mol. Life Sci.* **62**, 1234 (2005).

S32. U. Romling, M. Rohde, A. Olsen, S. Normark, J. Reinkoster, *Mol. Microbiol.* **36**, 10 (2000).

S33. U. Romling, W. D. Sierralta, K. Eriksson, S. Normark, *Mol. Microbiol.* **28**, 249 (1998).

S34. N. T. Chirwa, M. B. Herrington, *Microbiology* **149**, 525 (2003).

S35. M. A. Larkin *et al.*, *Bioinformatics* **23**, 2947 (2007).

S36. P. Gouet, E. Courcelle, D. I. Stuart, F. Metoz, *Bioinformatics* **15**, 305 (1999).

S37. A. D. Tischler, A. Camilli, *Mol. Microbiol.* **53**, 857 (2004).

S38. L. Holm, S. Kaariainen, P. Rosenstrom, A. Schenkel, *Bioinformatics* **24**, 2780 (2008).

S39. V. de Lorenzo, K. N. Timmis, *Methods Enzymol.* **235**, 386 (1994).

S40. F. H. Yildiz, G. K. Schoolnik, *Proc. Natl. Acad. Sci. U.S.A.* **96**, 4028 (1999).

S41. L. M. Guzman, D. Belin, M. J. Carson, J. Beckwith, *J. Bacteriol.* **177**, 4121 (1995).

Figure S1: Conservation of VpsT homologs in related *Vibrio* species. (A) Sequence alignment of VpsT homologs from various *Vibrio* species generated with ClustalW2 (*S35*) and formatted with ESPript (*S36*). Key residues responsible for c-di-GMP binding, nucleotide-dependent, and constitutive dimerization are marked with closed arrows. Asterisks highlight residues directly involved in coordination of c-di-GMP. Open arrows mark the degenerate phosphorylation switch, i.e. residues involved in magnesium coordination, phosphorylation, and phosphotransfer-dependent conformational changes in canonical REC domains. The following sequences were used to generate the alignment: *Vibrio cholerae* O1 biovar *El Tor* str. N16961 (NP_252391), *Vibrio parahaemolyticus* 16 (ZP_05117817), *Vibrio parahaemolyticus* RIMD 2210633 (NP_800957), *Vibrio harveyi* ATCC BAA-1116 (ABU73058), *Vibrio fischeri* ES114 (YP_205791), *Vibrio shilonii* AK1 (ZP_01865459), *Vibrio alginolyticus* 12G01 (ZP_01258564), *Vibrio sp.* Ex25 (ZP_04922131), *Vibrio vulnificus* YJ016 (NP_936438). **(B)** Sequence conservation mapped onto the solvent-accessible surface of VpsT. Conservation is presented as a color gradient from green to red (0%-100% conservation). Arrows and circles highlight structurally and functionally important motifs. **(C)** Surface conservation mapping based on alignment including VpsT-like protein sequences. As previously discussed, the latter carry a proline substitution at position 3 of the c-di-GMP binding pocket (W[L/F/M]PR) (not shown in the alignment in A). The surface shows significantly less conservation, especially in the interaction interfaces suggesting subfamily-specific dimerization.

Figure S2: Cyclic di-GMP dependence of VpsT-mediated gene transcription. *vpsL* gene expression in different genetic backgrounds harboring a single-copy chromosomal

vpsLp-lacZ fusion. Data are mean of 8 replicates -/+ SD. In this experiment, a smooth wild-type or *vpsT*-deletion strain was used that have low levels of c-di-GMP (*S2*). Induced expression of an active diguanlylate cyclase increases cellular c-di-GMP concentration (*S2, S37*). *vpsL* expression was driven to a large extent by VpsT in a c-di-GMP-dependent manner. A smaller fraction is independent of VpsT but requires an elevated c-di-GMP level. Although the analysis may be complicated by the usage of different genetic backgrounds, which may explain the differences in magnitude of *vpsL* expression comparing uninduced and induced samples, the data is supported by and consistent with other experiments described here that demonstrate that c-di-GMP and VpsT act in concert.

Figure S3: Dimerization and nucleotide-binding interfaces. (A) The c-di-GMP-independent dimerization interface. A crystallographic dimer is shown in cartoon presentation (chain A-chain B^{sym}) (left). The close-up view shows the dimerization interface (right). Interfacial residues are shown as sticks and labeled appropriately, where A and asterisk (*) identify residues belonging to chain A and chain B^{sym}, respectively. Pair-wise interactions spanning the interface are also denoted. **(B)** c-di-GMP-dependent interactions. A crystallographic dimer formed by two protomers in one asymmetric unit (chain A-chain B) is shown in cartoon presentation (left). The interaction is mediated primarily through helices α6 of each chain and is stabilized by the coordination of an intercalated c-di-GMP dimer at the base. A close-up view shows the protein interface (top-right). The second close-up view shows the c-di-GMP binding pocket (bottom-right). Protein interface residues, as well as residues participating in electrostatic and π-

stacking interactions with the nucleotide are depicted as sticks and appropriately labeled. Conservation of key residues participating in the formation of each interface is shown in the table at the bottom.

Figure S4: Isothermal titration calorimetry supports c-di-GMP binding *in vitro.* (A) Wild-type (wt) VpsT binds c-di-GMP with an apparent affinity in the low micromolar range (K_d ~ 3.2 μM). Binding occurs with a 1:1 stoichiometry in an entropically unfavorable (ΔS ~ -34 kcal/mole) exothermic reaction (ΔH ~ $-1.7x10^4$ kcal/mole). The top panel shows baseline-corrected data collected at 20°C, while the bottom shows the results of curve-fitting using a single/independent site binding model. **(B)** Baseline corrected data collected at 20°C for the $VpsT^{M17D}$, $VpsT^{R134A}$, $VpsT^{I141E}$, $VpsT^{W131F}$, $VpsT^{W131A}$, $VpsT^{T133A}$ and $VpsT^{T133V}$ mutants. While $VpsT^{M17D}$ complexes c-di-GMP with similar to wild-type affinity (K_d ~ 2.8 μM) and $VpsT^{T133A}$ with slightly reduced affinity (K_d ~ 7.4 μM), nucleotide binding was not detectable for the other VpsT mutants.

Figure S5: VpsT oligomerization state in solution. (A) Wild-type VpsT. The gel filtration profile of nucleotide-free, wild-type (wt) VpsT is characterized by a concentration-dependent shift in the elution peak (box). The protein concentration range is indicated as injected onto the column. SEC-coupled multi-angle light scattering analysis of wild-type VpsT in presence (middle) and absence (left) of c-di-GMP are shown. The signal from the 90°-scattering detector is shown in color, the signal from the refractive index detector is shown as dashed line and the UV absorbance is plotted in grey. Average molecular weights are plotted in black against the right Y-axis, as

calculated every second across the protein elution peak. Theoretical molecular weights corresponding to those of a monomer and a dimer are indicated as horizontal dashed, grey lines. Rapid equilibria between monomers and dimeric assemblies are detected as species with intermediate molecular weights. Experiments evaluating the effects of c-di-GMP were conducted after pre-incubation with excess nucleotide, followed by separation in a mobile phase lacking c-di-GMP. Injected protein and nucleotide concentrations were 400 μM and 600 μM, respectively. **(B)** $VpsT^{M17D}$. The mutant was analyzed as described above. In addition, experiments were carried out with 40 μM c-di-GMP in running buffer (right) to stabilize the VpsT•c-di-GMP complex during SEC. **(C)** $VpsT^{R134A}$. The mutant was analyzed as described in A and B. Asterisks denote small molecule peaks in the UV absorbance, plausibly due to the elution of unbound nucleotide. **(D)** $VpsT^{I141E}$. The mutant was analyzed as described above. Results were similar to those obtained with $VpsT^{R134A}$. Results from SEC-coupled multi-angle light scattering and ITC are summarized in Table S2. The monomeric molecular weight obtained with $VpsT^{M17D}$ compared to higher molecular weights for the rest of the mutants and the wild-type protein indicates constitutive VpsT dimerization through the nucleotide-independent interface in the absence of nucleotide. Increased molecular weights and shifts in the elution peaks for the wild-type and $M^{17}D$ proteins in the presence of c-di-GMP are indicative of a nucleotide-dependent change in oligomerization through the corresponding interface.

Figure S6: Analytical ultracentrifugation of wild-type VpsT. VpsT was analyzed by sedimentation velocity analytical ultracentrifugation at 8 and 12 μM protein

concentration in the presence and absence of c-di-GMP (25 μM). Molecular weights were analyzed by using the program SedFit.

Figure S7: Functional analysis of VpsT with mutations at the putative phosphorylation site. (A) Whole genome expression profiling. Top, compact heatmap in a log2-based pseudocolor scale (yellow, induced; blue, repressed) comparing differentially expressed genes in a Δ*vpsT* strain expressing wild-type (wt) or mutated VpsT versions compared to the vector control (midpanel, expression profiles of *vps*-I and *vps*-II clusters and genes encoding matrix proteins; bottom, expression profiles of flagellar biosynthesis genes). **(B)** Quantitative PCR for *flaA* expression. Expression of *flaA* in a *vpsT*-deletion strain (Δ*vpsT*) expressing wild-type (wt) and mutant VpsT proteins from a pBAD plasmid. Concentration of the inducer arabinose is 0.1% as used in the β-galactosidase and expression profiling assays. Expression of the housekeeping *gyrA* gene is used for normalization. Data are mean of 3 replicates -/+ SD. **(C)** Motility phenotypes on semisolid LB agar plates. For strains expressing mutants of VpsT, single chromosomal insertion mutants are shown. The graph shows the mean migration zone diameter of each strain. Data are mean of 8 replicates -/+ SD. **(D)** Spot morphology. A wild-type rugose strain carrying the vector (pBAD) and Δ*vpsT* strains carrying the vector or plasmids containing wild-type or mutant *vpsT* are shown (bars=1 mm). Mutations in the putative phosphorylation site designed to produce a constitutively inactive or active state, $VpsT^{D60A}$ and $VpsT^{D60E}$, respectively, show identical phenotypes indicating that phosphorylation is unlikely a regulatory mechanism for VpsT function.

Figure S8: Spot morphology phenotypes for additional nucleotide binding mutants of VpsT. A wild-type rugose strain carrying the vector (pBAD) or a plasmid containing wild-type VpsT, and Δ*vpsT* strains carrying the vector or plasmids containing wild-type or mutant *vpsT* are shown (top, unscaled; bottom, scaled to similar diameter, bars=1 mm). The double VpsT$^{M17D/R134A}$ mutant shows a phenotype observed for the single VpsT^{R134A} and VpsT^{I141E} mutants, indicating that c-di-GMP-driven dimerization is dominant in VpsT function. The boxed inset shows *vpsL* gene expression in different genetic backgrounds harboring a single-copy chromosomal *vpsLp-lacZ* fusion. Data are mean of 8 replicates -/+ SD.

Figure S9: Comparison of c-di-GMP-bound and nucleotide-free VpsT. (A) Asymmetric unit and crystal packing. The asymmetric unit contains four VpsT protomers (cartoon presentation), and is shown for the c-di-GMP-bound VpsT crystal. Adjacent symmetry mates are shown in transparent surface presentation illustrating the polymerization of VpsT in the crystals mediated by the c-di-GMP-stabilized and nucleotide-independent interfaces. Interfacial surface areas and interaction free energy gain estimations were calculated using the PISA server (*S17*). **(B)** Structural comparison of VpsT promoters. Superposition of the α-carbon backbone of all 8 symmetry-unrelated protomers in the unliganded and complex crystal structures of VpsT shows almost identical protein conformation (rmsd of 0.5-0.9Å over all atoms). **(C)** Structural comparison of oligomeric assemblies of c-di-GMP-bound and nucleotide-free VpsT. Superposition of the corresponding crystallographic trimers using molecule A as the reference shows minor adjustments in the packing (top), where the VpsT protomers move

as rigid bodies. A close-up view of the c-di-GMP binding site shows alternative rotamer conformation for arginine R^{134}, as well as narrowing of the nucleotide-binding pocket in the apo-state (bottom).

Figure S10: Structure of a REC domain structurally related to VpsT. (A) Crystal structure of the receiver domain of a LuxR-like response regulator from *Aurantimonas sp. SI85-9A1* (PDB code 3cz5; Malashkevich et al.; unpublished). A DALI search identified the aforementioned protein as a structural homolog to VpsT (*S38*). Similarly to VpsT, this receiver domain contains an additional helix α6, mediating dimerization contacts in the crystal lattice (top). However, no ligand is stabilizing the interaction, and a bound phosphate ion at the putative phosphorylation site (bottom) suggests control by phosphorylation. Residues involved in magnesium binding, phosphorylation, and phosphotransfer-dependent conformational changes are depicted as sticks and appropriately labeled. The phosphate ion bound at the putative phosphorylation site is shown as spheres. **(B)** Conservation of residues involved in phosphotransfer as compared to canonical (WspR and PhoB) and divergent (CsgD and VpsT) receiver domains. Residue numbers in the table correspond to the VpsT sequence.

Figure S11: Conserved residues form a path through the REC domain connecting the c-di-GMP-independent interface and the c-di-GMP binding site. (A) Structure of the receiver domain dimer showing c-di-GMP bound at the base of helices α6. **(B)** Close-up view of the putative phosphorylation site. Residues involved in phosphotransfer in canonical receiver domains are shown as sticks, as well as residue M^{17} from an adjacent

molecule, stabilizing the constitutive dimer interface, and residue W^{131} from the c-di-GMP binding pocket (top). Conserved residues connecting the c-di-GMP-independent interface and the nucleotide binding site are shown in magenta. Interestingly, these include the degenerate phosphorylation site together with residues involved in phosphotransfer-related conformational switching, suggesting that they might form an allosteric path for phosphorylation-dependent α6 dimerization in other LuxR-like response regulators (see Figure S10).

Figure S12: Models for DNA binding to VpsT. (A) Nucleotide-independent VpsT dimer. The dimer is shown in two views that are separated by a 45°-rotation along the x-axis. The structure of the HTH domain of NarL bound to cognate DNA (*S16*) was superimposed onto the HTH domain of VpsT to illustrate the DNA binding mode of VpsT dimers. **(B)** Cyclic di-GMP-stabilized VpsT dimer. The dimer is shown in two orthogonal views. DNA binding was modeled as described above. **(C)** Tetrameric models of VpsT•DNA complexes. Based on the crystal packing contacts, two plausible tetrameric assemblies can be constructed. In the left panel, c-di-GMP bridges two nucleotide-independent dimers. The DNA was used from a structure of the catabolite activator protein, a transcriptional regulator that bends DNA in a 90°-angle (*S21*). In the right panel, two c-di-GMP-driven dimers associate via the nucleotide-independent dimerization interface of VpsT. The central DNA is taken from a catabolite activator protein•DNA complex structure, the lateral DNA fragments are taken from a NarL•DNA complex structure. The distribution of VpsT binding sites on the chromosomes is likely to determine the feasibility of these models for transcriptional regulation.

Figure S13: Quantitative PCR (qPCR) results show modest VpsT overexpression. Expression of wild-type (wt) and mutant VpsT proteins from a pBAD plasmid introduced in a *vpsT*-deletion strain (Δ*vpsT*) is compared to chromosome-driven VpsT expression in the wild-type rugose strain carrying an insert-less vector. Concentration of the inducer arabinose is 0.1% as used in the β-galactosidase and expression profiling assays. Expression of the housekeeping *gyrA* gene is used for normalization. Data are mean of 3 replicates -/+ SD.

Table S1. Data collection and refinement statistics.

Data collection	**VpsT•c-di-GMP**	**VpsT (nucleotide free)**		
X-ray source	NSLS, X29	NSLS, X29	NSLS, X29	NSLS, X29
Wavelength (Å)	1.0809	0.9788 (peak)	0.9794 (inflection)	1.0809 (remote)
Space group	$P4_12_12$	$P4_12_12$	$P4_12_12$	$P4_12_12$
Unit cell parameters				
a, b, c (Å)	121.7, 121.7, 208.2	121.4, 121.4, 198.4	121.4, 121.4, 198.9	121.9, 121.9, 199.2
α, β, γ (°)	90, 90, 90	90, 90, 90	90, 90, 90	90, 90, 90
Resolution range (Å)	50.0-2.8 (2.97-2.8)[a]	50.0-3.1 (3.27-3.1)	50.0-3.2 (3.35-3.2)	50.0-3.4 (3.65-3.4)
No. of reflections				
Total	555982 (88936)	521519 (76688)	475332 (61878)	329892 (39399)
Unique	38433 (6048)	52138 (8187)	47985 (7137)	32884 (4451)
Completeness (%)	97.8 (97.3)	99.2 (96.7)	98.2 (90.8)	86.4 (72.7)
Redundancy	14.5 (14.7)	10.0 (9.4)	9.9 (8.7)	10.0 (8.8)
$I/\sigma(I)$	18.2 (4.0)	11.8 (3.2)	12.5 (3.7)	14.8 (5.3)
R_{meas} (%)	11.7 (78.8)	13.1 (84.3)	11.8 (66.7)	11.5 (48.1)
Refinement				
R_{work}/R_{free} (%)	24.6/29.0	24.8/30.8		
r.m.s. deviations				
Bond length (Å)	0.007	0.011		
Bond angles (°)	1.049	1.271		
No. of atoms				
Protein	6649	6640		
Water	49	---		
c-di-GMP/Tartrate	184/20	---		
Ave. B-factors (Å^2)				
Protein	54.6	74.6		
Water	41.2	---		
c-di-GMP/Tartrate	38.5/56.8	---		
Ramachandran (%)[b]				
Favored	90.4	89.7		
Allowed	9.0	9.9		
Generous	0.7	0.4		
Disallowed	0.0	0.0		

(a) Values for the highest resolution bin. (b) Calculated with PROCHECK.

Table S2. Oligomeric state and c-di-GMP affinity of VpsT.

Protein	Property	- c-di-GMP	+ c-di-GMP	
			Preincubation	/ In SEC buffer
$VpsT^{wt}$				
	Molecular weight (MALS)	42.3 kDa	52.6 kDa	/ n.a.
	Polydispersity (MALS)	1.006 ± 0.03	1.004 ± 0.03	/ n.a.
	c-di-GMP binding affinity / stoichiometry (ITC)		3.18 ± 0.94 μM	
$M^{17}D$				
	Molecular weight (MALS)	25.9 kDa	35.1 kDa	/ 44.0 kDa
	Polydispersity (MALS)	1.007 ± 0.08	1.008 ± 0.07	/ 1.003 ± 0.04
	c-di-GMP binding affinity / stoichiometry (ITC)		2.81 ± 1.06 μM	
$R^{134}A$				
	Molecular weight (MALS)	41.5 kDa	41.8 kDa	/ 40.5 kDa
	Polydispersity (MALS)	1.008 ± 0.05	1.005 ± 0.05	/ 1.001 ± 0.04
	c-di-GMP binding affinity (ITC)		n.d.	
$I^{141}E$				
	Molecular weight (MALS)	40.6 kDa	40.8 kDa	/ 40.4 kDa
	Polydispersity (MALS)	1.004 ± 0.05	1.003 ± 0.05	/ 1.003 ± 0.04
	c-di-GMP binding affinity (ITC)		n.d.	
BSA				
	Molecular weight (MALS)	63.8 kDa	n.a.	/ 64.1 kDa
	Polydispersity (MALS)	1.001 ± 0.02	n.a.	/ 1.001 ± 0.03

Table S3. Gene expression profiles. Differenty expressed genes (≥2-fold) in rugose Δ*vpsT* harboring *vpsT*-WT, *vpsT*-M17D, *vpsT*-D60A, *vpsT*-R134A or *vpsT*-I141E in comparison to the same strain containing pBAD alone. Differentially expressed genes were determined using SAM software, with criteria of a ≥2-fold change in gene expression and a false discovery rate of ≤3%.

Open Reading Frame and Functional Category	Gene	Function	*vpsT*-WT	*vpsT*-M^{17}D	*vpsT*-D^{60}A	*vpsT*-R^{134}A	*vpsT*-I^{141}E
Biofilm Related Functions							
VC0916	*vpsU*	phosphotyrosine protein phosphatase	2.57	4.70	3.40		
VC0917	*vpsA*	UDP-N-acetylglucosamine 2-epimerase	3.02	6.21	3.80		
VC0918	*vpsB*	UDP-N-acetyl-D-mannosaminuronic acid dehydrogenase	3.29	8.27	5.44	2.18	
VC0919	*vpsC*	serine acetyltransferase-related protein	3.28	6.50	4.70		
VC0920	*vpsD*	exopolysaccharide biosynthesis protein	2.19	3.83	2.36		
VC0921	*vpsE*	polysaccharide export protein		2.36	2.13		
VC0922	*vpsF*	hypothetical protein	2.66	4.92	3.52		
VC0924	*vpsH*	capK protein putative	2.71	4.91	3.53		
VC0925	*vpsI*	polysaccharide biosynthesis protein	2.55	5.32	3.75		
VC0926	*vpsJ*	hypothetical protein	4.03	5.89	4.88		
VC0927	*vpsK*	UDP-N-acetyl-D-mannosamine transferase	2.41	3.70	3.09		
VC0928	*rbmA*	hypothetical protein	7.36	8.80	5.24		
VC0930	*rbmB*	hemolysin-related protein		2.20			
VC0931	*rbmC*	conserved hypothetical protein	9.50	4.82	2.93		
VC0932	*rbmD*	hypothetical protein	12.30	10.45	5.91		
VC0933	*rbmE*	hypothetical protein	3.83	3.87	3.05		
VC0934	*vpsL*	capsular polysaccharide biosynthesis glycosyltransferase	2.46	2.50			
VC0935	*vpsM*	hypothetical protein	19.14	19.72	11.95		
VC0936	*vpsN*	polysaccharide export-related protein	18.79	16.67	9.32		
VC0937	*vpsO*	exopolysaccharide biosynthesis protein	5.83	5.22	3.20		
VC0938	*vpsP*	hypothetical protein	2.91	2.01			
VC1029	*cdgB*	cyclic-di-guanylate protein	2.15				
VC1888	*bap1*	hemolysin-related protein	2.14	3.84	2.69		
VC2455	*vpvB*	*Vibrio* phase variation protein		7.09	3.64		
VC2456	*vpvA*	*Vibrio* phase variation protein		4.12	2.52		
VCA0074	*cdgA*	GGDEF family protein		2.09			
VCA0075	VCA0075	hypothetical protein		2.17			
Chemotaxis and Motility							
VC1298	VC1298	methyl-accepting chemotaxis protein	0.40				
VC1413	VC1413	methyl-accepting chemotaxis protein	0.32	0.17			
VC1763	VC1763	chemotaxis protein MotB-related protein		0.50			
VC1898	VC1898	methyl-accepting chemotaxis protein		0.35			
VC2065	*cheY*-3	chemotaxis protein		0.48			
VC2068	*flhF*	flagellar biosynthetic protein		0.34			
VC2069	*flhA*	flagellar biosynthetic protein		0.31			
VC2131	*fliH*	flagellar assembly protein		0.48			
VC2132	*fliG*	flagellar motor switch protein		0.47			
VC2133	*fliF*	flagellar M-ring protein		0.41			
VC2134	*fliE*	flagellar hook-basal body complex protein		0.26	0.41		

VC2142	*flaB*	flagellin		0.40	0.45		
VC2143	*flaD*	flagellin	0.37	0.20	0.25		
VC2187	*flaC*	flagellin		0.26			
VC2188	*flaA*	flagellin core protein	0.42	0.27	0.34		
VC2189	VC2189	hypothetical protein	0.18	0.15	0.31		
VC2191	*flgM*	flagellar hook-associated protein		0.28			
VC2194	*flgH*	flagellar L-ring protein		0.41			
VC2195	*flgG*	flagellar basal-body rod protein	0.47	0.25	0.43		
VC2196	*flgF*	flagellar basal-body rod protein		0.37			
VC2197	*flgE*	flagellar hook protein		0.28			
VC2198	*flgD*	basal-body rod modification protein		0.45			
VC2199	*flgC*	flagellar basal-body rod protein		0.36			
VC2200	*flgB*	flagellar basal-body rod protein		0.21	0.32		
VCA0864	VCA0864	methyl-accepting chemotaxis protein		2.29			
Hypothetical							
VC0102	VC0102	hypothetical protein	0.48				
VC0132	VC0132	hypothetical protein			2.89		
VC0138	VC0138	hypothetical protein		2.46			
VC0184	VC0184	hypothetical protein	2.08				
VC0283	VC0283	hypothetical protein		2.11			
VC0823	VC0823	hypothetical protein					0.50
VC1420	VC1420	hypothetical protein		0.47			
VC1538	VC1538	hypothetical protein	0.34				
VC1933	VC1933	hypothetical protein	0.48				
VC1997	VC1997	hypothetical protein			2.05		
VC2046	VC2046	hypothetical protein		0.44			
VC2058	VC2058	hypothetical protein		0.49			
VC2207	VC2207	hypothetical protein	0.46	0.21	0.45		
VC2304	VC2304	hypothetical protein					0.43
VC2331	VC2331	hypothetical protein	2.06	2.66			
VC2372	VC2372	hypothetical protein			6.07		
VC2667	VC2667	hypothetical protein		2.40			
VCA0215	VCA0215	hypothetical protein			2.72		
VCA0284	VCA0284	hypothetical protein		0.46			0.47
VCA0556	VCA0556	hypothetical protein		0.46			
VCA0672	VCA0672	hypothetical protein		0.48			
VCA0874	VCA0874	hypothetical protein		0.43			
VCA0934	VCA0934	hypothetical protein		0.43			
VCA0935	VCA0935	hypothetical protein	0.33	0.41			
VCA1075	VCA1075	hypothetical protein	0.27				
VCA1076	VCA1076	hypothetical protein	0.21				
VC1151	VC1151	conserved hypothetical protein	0.50				
VC1710	VC1710	conserved hypothetical protein	0.43				
VC2206	VC2206	conserved hypothetical protein		0.35			
VC2386	VC2386	conserved hypothetical protein		0.49			
VCA0055	VCA0055	conserved hypothetical protein	2.73	5.90	4.12		
VCA0167	VCA0167	conserved hypothetical protein		2.54	2.42		
VCA0536	VCA0536	conserved hypothetical protein	0.31				

Regulatory Functions							
VC0665	*vpsR*	sigma-54 dependent transcriptional regulator		2.18			
VC1118	VC1118	transcriptional regulator putative		0.40			
VC1349	VC1349	sensory box sensor histidine kinase/response regulator		2.03			
VCA0166	*cspA*	cold shock transcriptional regulator					0.46
VCA0933	VCA0933	cold shock domain family protein	0.41	0.39		0.39	0.37
Others							
VC0194	*ggt*	gamma-glutamyltranspeptidase		2.27			
VC0284	VC0284	TonB system receptor	2.57	4.51	3.11		
VC0436	*rpmA*	ribosomal protein L27					0.45
VC0475	*irgA*	enterobactin receptor			0.47		
VC0586	VC0586	carbonic anhydrase putative	0.50				
VC0679	*rpsT*	ribosomal protein S20	0.41				
VC1301	*sdaC*-1	serine transporter		2.23	2.04		
VC1584	*ankB*	ankB protein	2.25				
VC1585	*katB*	catalase	2.39	2.18			
VC1620	VC1620	hypothetical protein	0.33	0.36	0.42		
VC1621	VC1621	agglutination protein	0.41				
VC1622	VC1622	outer membrane protein putative	0.46				
VC1672	*tag*	DNA-3-methyladenine glycosidase I		4.55			
VC1862	VC1862	amino acid ABC transporter permease protein		0.48			
VC1935	VC1935	CDP-diacylglycerol--glycerol-3-phosphate 3-phosphatidyltransferase-related protein		2.06			
VC1936	VC1936	phosphatidate cytidylyltransferase putative		2.30			
VC2305	*ompK*	outer membrane protein	0.49				
VC2336	VC2336	methionyl-tRNA synthetase-related protein	2.42	2.43			
VC2416	VC2416	2, 3-cyclic-nucleotide 2-phosphodiesterase		2.31			
VC2582	*rpsH*	ribosomal protein S8	2.00				
VCA0057	*phrB*-2	deoxyribodipyrimidine photolyase	2.09	3.94	2.54		
VCA0064	*hutR*	heme receptor					2.02
VCA0088	*gltP*-2	proton/glutamate symporter	2.04				
VCA0518	*fruB*	PTS system fructose-specific			0.50		
VCA0860	*malS*	alpha-amylase			0.46		
VCA1028	*ompS*	maltoporin			0.34		

Table S4. Bacterial strains and plasmids.

Strain or plasmid	Relevant properties	Source
***E. coli* strain**		
DH10B	F$^-$ *mcrA* Δ(*mrr-hsdRMS-mcrBC*) ϕ80*lacZ*ΔM15 Δ*lacX74 recA1 endA1 ara*Δ*139* Δ(*ara leu*)*7697 galU galK* λ$^-$ *rpsL* (Str^r) *nupG*	Invitrogen
S17-1 (λ *pir)*	Tp^r Sm^r *recA, thi, pro,* r_K^- m_K^+ *RP4:2-Tc*:MuKm Tn7 λ *pir*	(*39*)
DH5α	*fhuA2*Δ*(argF-lacZ)U169 phoA glnV44* ϕ80 *lacZ*ΔM15 *gyrA96 recA1 relA1 endA1 thi-1 hsdR17*	NEB
T7 Express	*fhuA2 lacZ::T7 gene1 [lon] ompT gal sulA11 R(mcr-73::miniTn10--*Tet^S*)2 [dcm] R(zgb-210::Tn10--*Tet^S*) endA1* Δ*(mcrC-mrr)114::IS10*	NEB
T7 Express Crystal	*fhuA2 lacZ::T7 gene1 [lon] ompT gal sulA11 R(mcr-73::miniTn10--*Tet^S*)2 [dcm] R(zgb-210::Tn10--*Tet^S*) endA1 metB1* Δ*(mcrC-mrr)114::IS10*	NEB
***V. cholerae* strains**		
FY_Vc_1	*Vibrio cholerae* O1 El Tor A1552, smooth variant, Rif^r	(*40*)
FY_Vc_2	*Vibrio cholerae* O1 El Tor A1552, rugose variant, Rif^r	(*40*)
FY_Vc_616	FY_Vc_1 carrying chromosomal *vpsLp-lacZ*, Rif^r	(*3*)
FY_Vc_618	FY_Vc_2 carrying chromosomal *vpsLp-lacZ*, Rif^r	This study
FY_Vc_5	FY_Vc_2 Δ*vpsT*	(*4*)
FY_Vc_4435	FY_Vc_618 Δ*vpsT*	This study
FY_Vc_3463	FY_Vc_616 Δ*vpsT*	(*3*)
FY_Vc_5045	FY_Vc_618 carrying chromosomal *vpsT*(M17D)	This study
FY_Vc_5046	FY_Vc_618 carrying chromosomal *vpsT*(D60A)	This study
FY_Vc_5047	FY_Vc_618 carrying chromosomal *vpsT*(D60E)	This study
FY_Vc_5048	FY_Vc_618 carrying chromosomal *vpsT*(R134A)	This study
FY_Vc_5049	FY_Vc_618 carrying chromosomal *vpsT*(I141E)	This study
Plasmids		
pET28a/His-*sumo*	modified pET28a (Novagen) yielding N-terminally hexahistidine-tagged SUMO fusion proteins, Kan^r	This study
pETsumo_wt	pET28a/His-*sumo*::*vpsT*, Kan^r	This study
pETsumo_M^{17}D	pET28a/His-*sumo*::*vpsT*(M17D), Kan^r	This study
pETsumo_R^{134}A	pET28a/His-*sumo*::*vpsT*(R134A), Kan^r	This study
pETsumo_I^{141}E	pET28a/His-*sumo*::*vpsT*(I141E), Kan^r	This study
pETsumo_W^{131}F	pET28a/His-*sumo*::*vpsT*(W131F), Kan^r	This study
pETsumo_W^{131}A	pET28a/His-*sumo*::*vpsT*(W131A), Kan^r	This study
pETsumo_T^{133}A	pET28a/His-*sumo*::*vpsT*(T133A), Kan^r	This study
pETsumo_T^{133}V	pET28a/His-*sumo*::*vpsT*(I133V), Kan^r	This study
pBAD/*myc*-His-B	Arabinose-inducible expression vector with C-terminal myc epitope and six-His tags, Ap^r	Invitrogen
pFY-876	pBAD/*myc*-His-B::*vpsT*, Ap^r	This study
pFY-877	pBAD/*myc*-His-B::*vpsT*(M17D), Ap^r	This study
pFY-842	pBAD/*myc*-His-B::*vpsT*(W131F), Ap^r	This study
pFY-881	pBAD/*myc*-His-B::*vpsT*(T133A), Ap^r	This study
pFY-843	pBAD/*myc*-His-B::*vpsT*(T133V), Ap^r	This study
pFY-844	pBAD/*myc*-His-B::*vpsT*(R134A), Ap^r	This study

pFY-846	pBAD/*myc*-His-B::*vpsT*(I141E), Ap^r	This study
pFY-884	pBAD/*myc*-His-B::*vpsT*(M17D/R134A), Ap^r	This study
pFY-903	pBAD/*myc*-His-B::*vpsT*(D60A), Ap^r	This study
pFY-904	pBAD/*myc*-His-B::*vpsT*(D60E), Ap^r	This study
pFY-217	pGP704-*sacB*28::*vpsLp-lacZ* transcriptional fusion; Ap^r	(*10*)
pBAD33	pACYC184 ori, araC P_{araBAD}, Cm^r	(*41*)
pAT1662	pBAD33::VCA0956-His_6, Cm^r	(*37*)
pFY-959	pGP704-*sacB*28::*vpsT*(M17D), Ap^r	This study
pFY-960	pGP704-*sacB*28::*vpsT*(D60A), Ap^r	This study
pFY-961	pGP704-*sacB*28::*vpsT*(D60E), Ap^r	This study
pFY-962	pGP704-*sacB*28::*vpsT*(R134A), Ap^r	This study
pFY-963	pGP704-*sacB*28::*vpsT*(I141E) Ap^r	This study

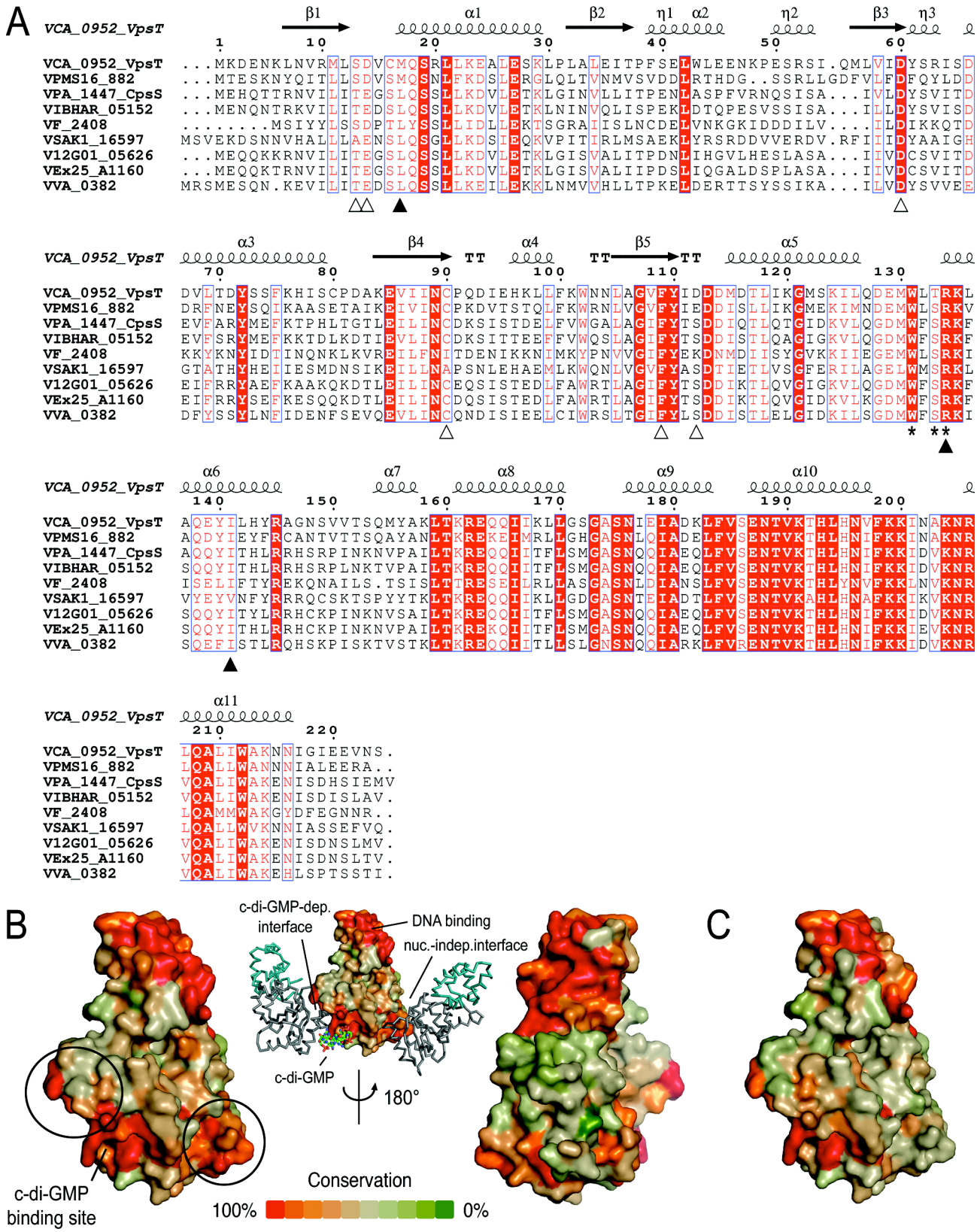

Figure S1: Krasteva *et al.*

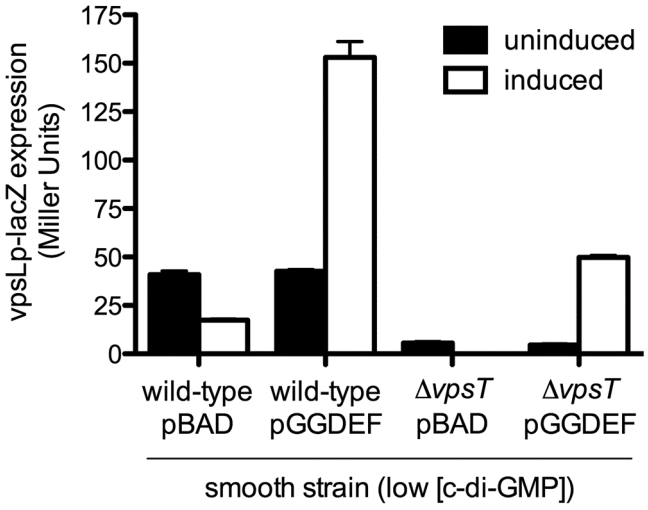

Figure S2: Krasteva *et al.*

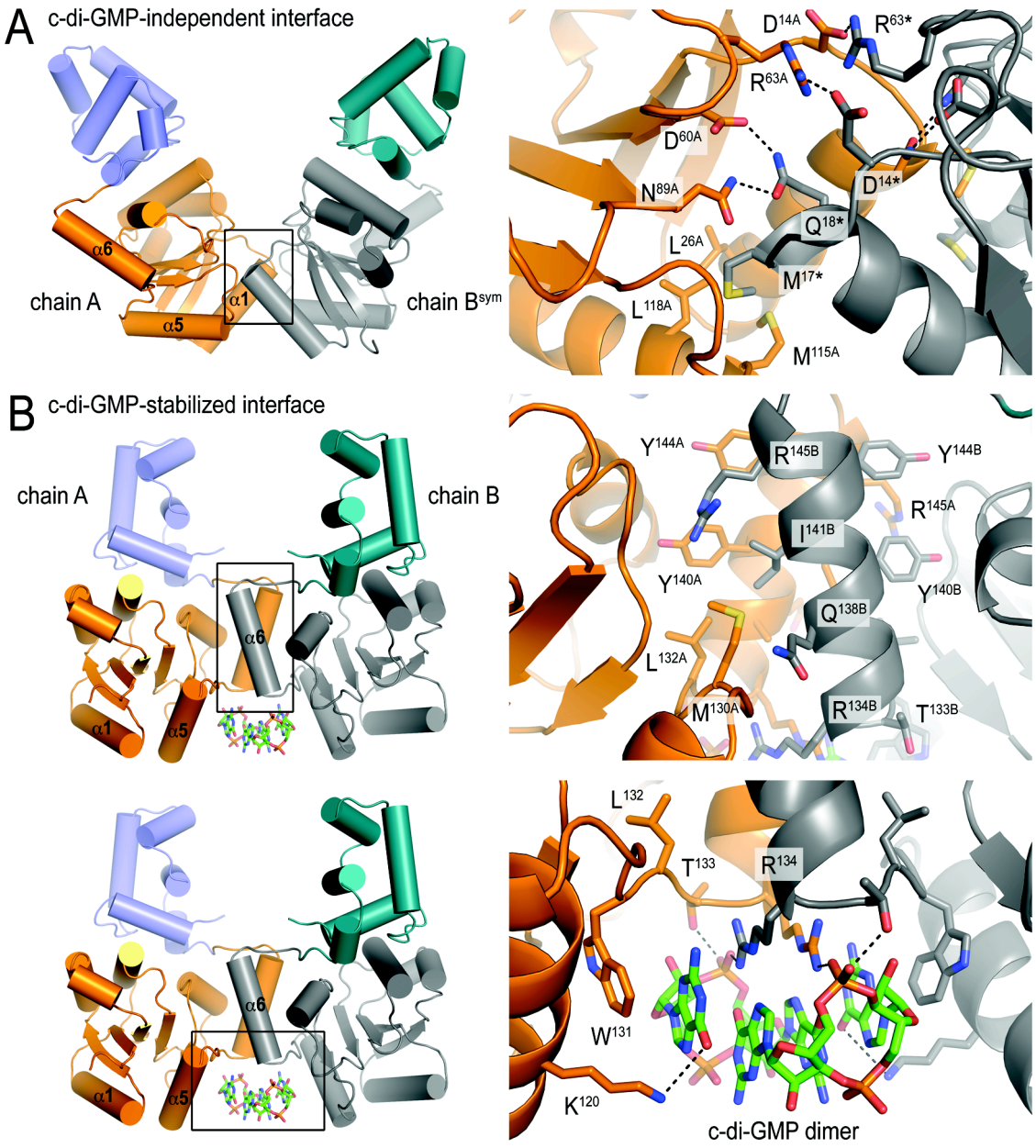

	17	131	132	133	134	141
VpsT (e.g. VCA0952)	[M/L]	W	[L/F/M]	[T/S]	R	[I/V]
VpsT-like (e.g. VC0396)	n.c.	W	[L/F/M]	P	R	[I/L]
CsgD (E. coli)	L	Y	F	[T/S]	Q	I

Figure S3: Krasteva *et al.*

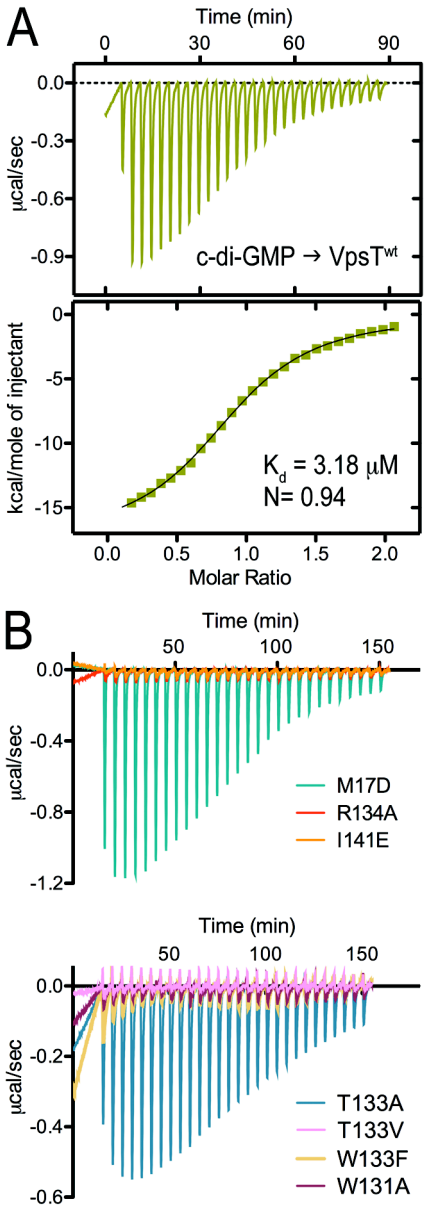

Figure S4: Krasteva *et al.*

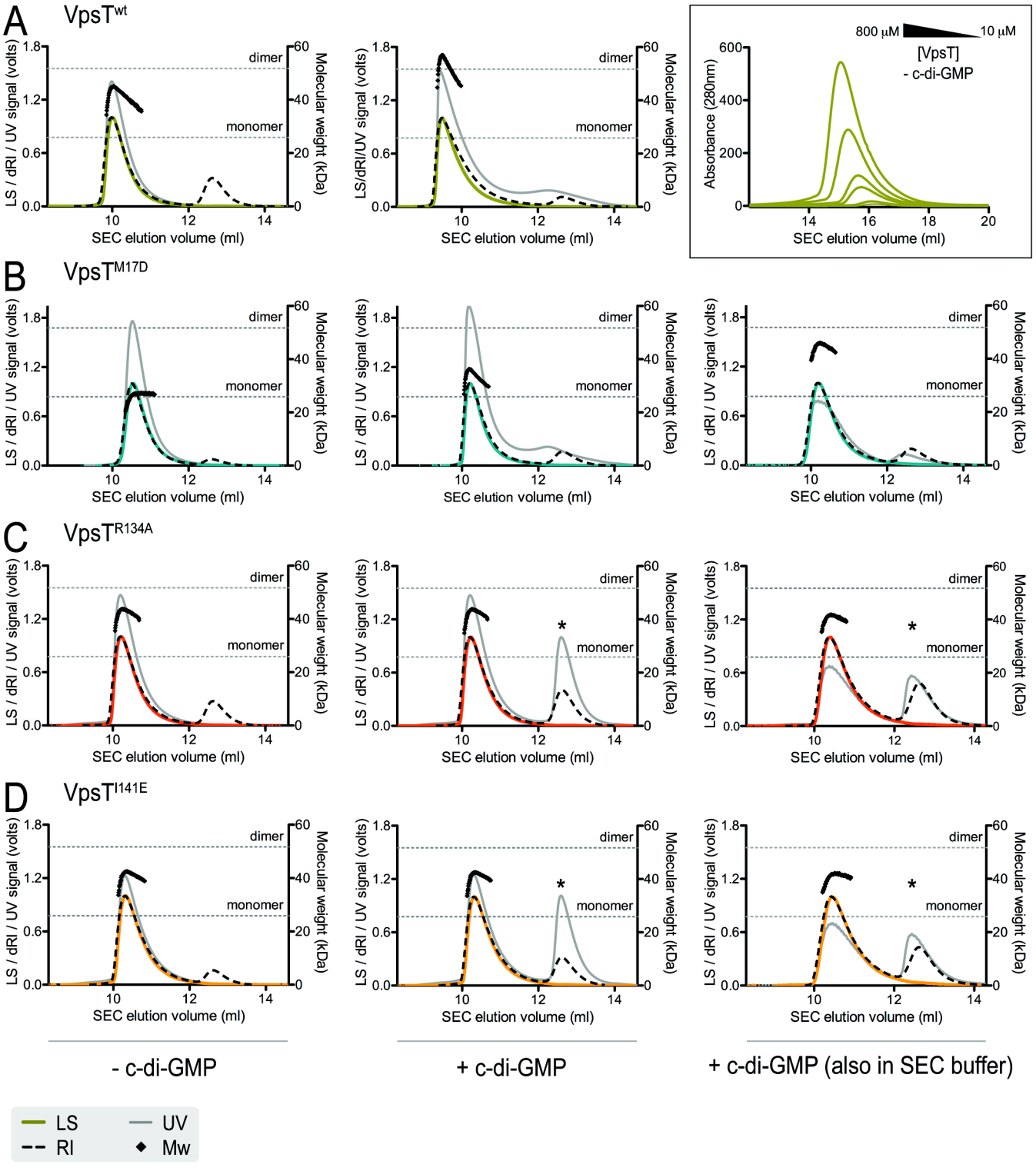

Figure S5: Krasteva *et al.*

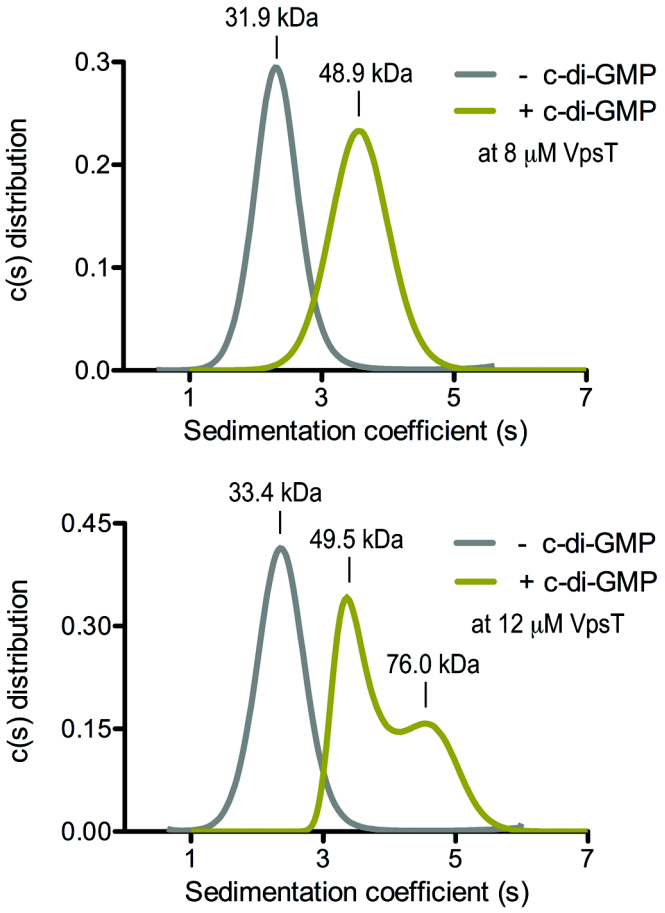

Figure S6: Krasteva *et al.*

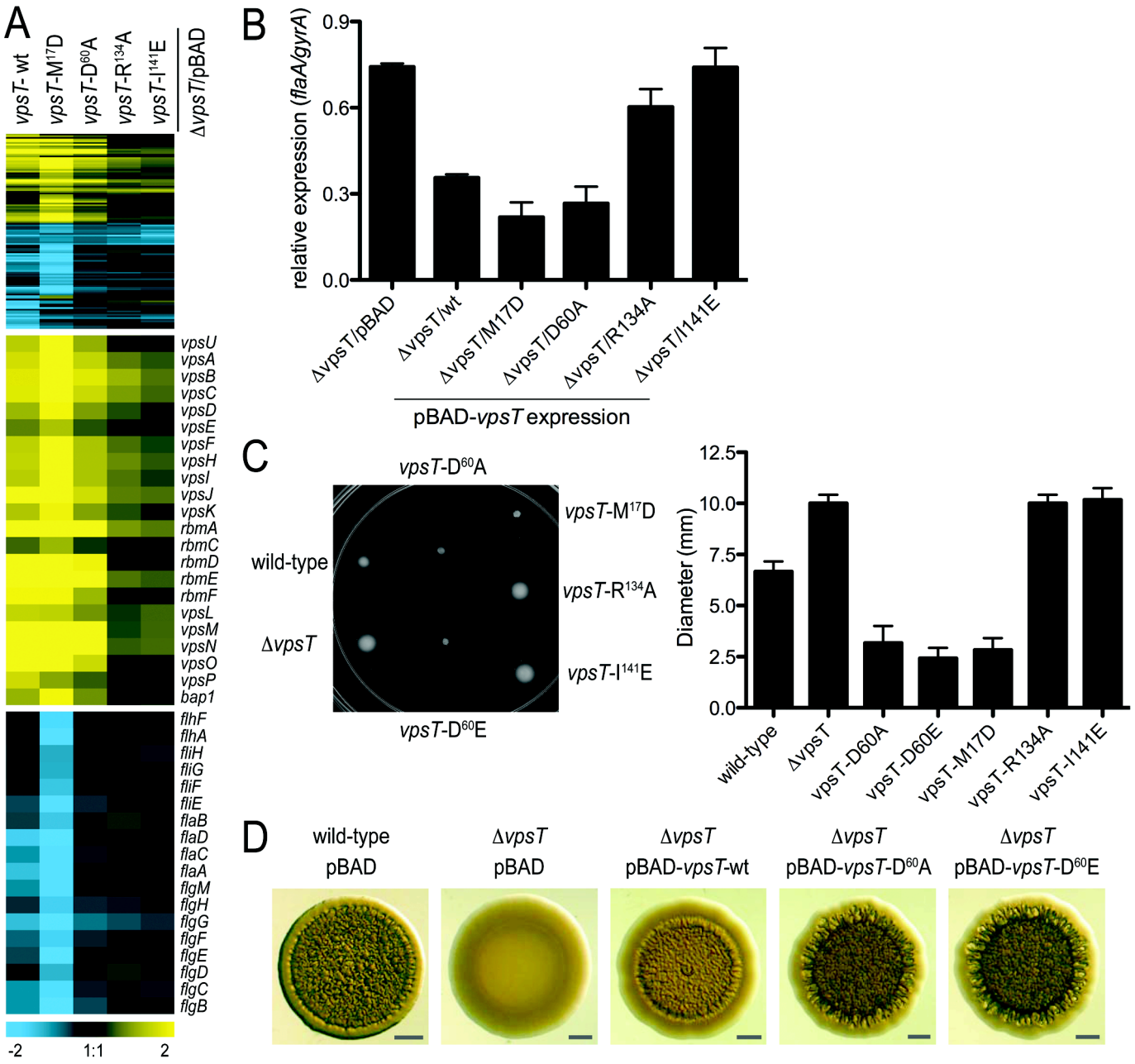

Figure S7: Krasteva *et al.*

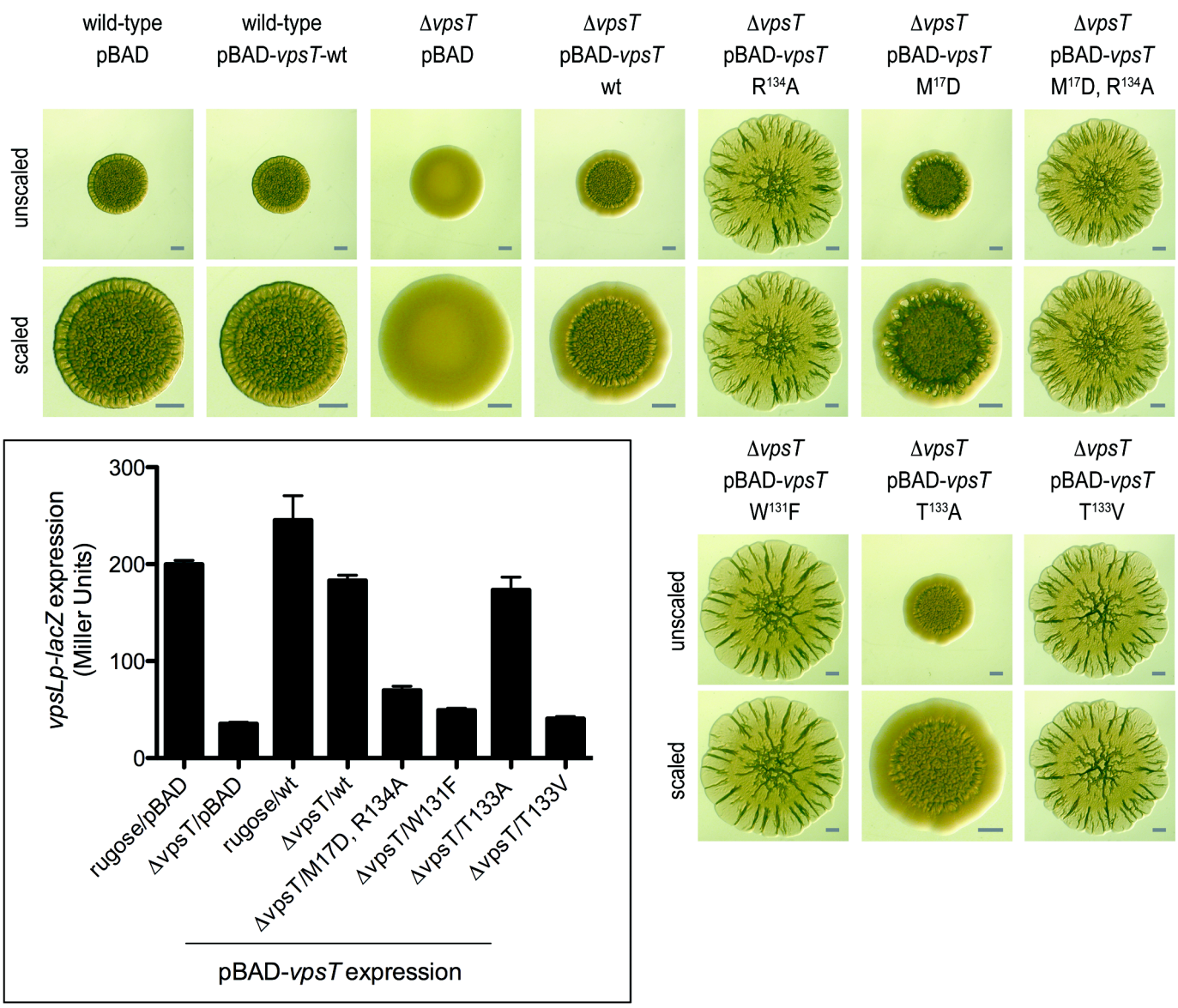

Figure S8: Krasteva *et al.*

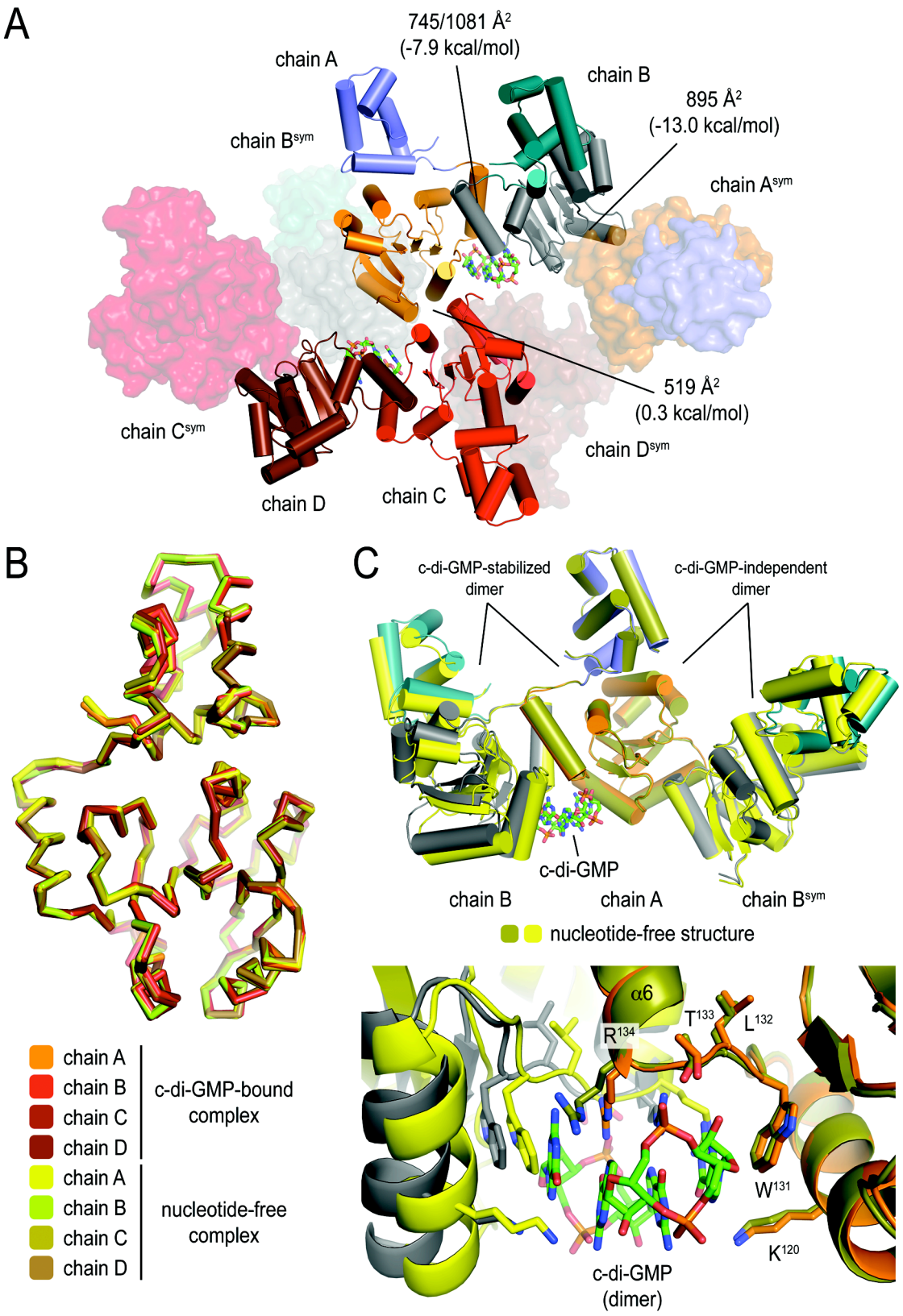

Figure S9: Krasteva *et al.*

A

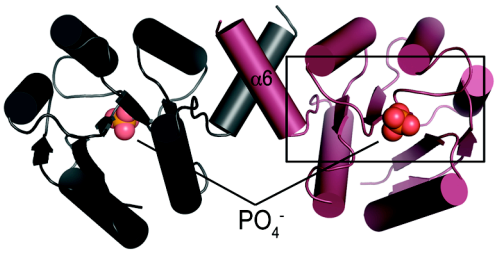

PDB code: 3cz5

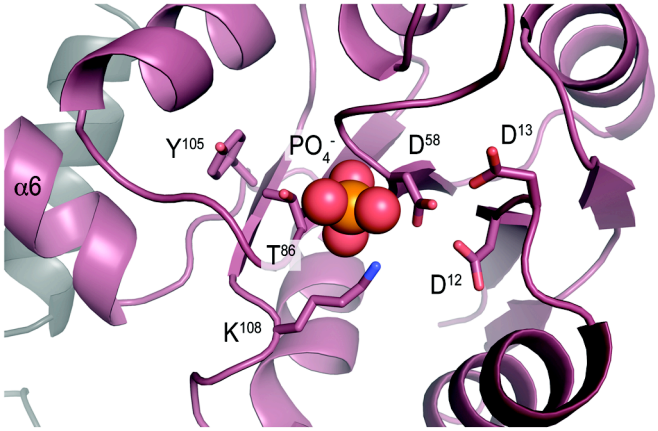

B

	13 14	60 112	90 109
VpsT	S D	D -//- D	C -//- F
CsgD	T K	D -//- M	T -//- F
3cz5	D D	D -//- K	T -//- Y
WspR	D D	D -//- K	S -//- Y
PhoB	E D	D -//- K	T -//- Y
	Mg^{2+}	phosphate	switch

Figure S10: Krasteva *et al.*

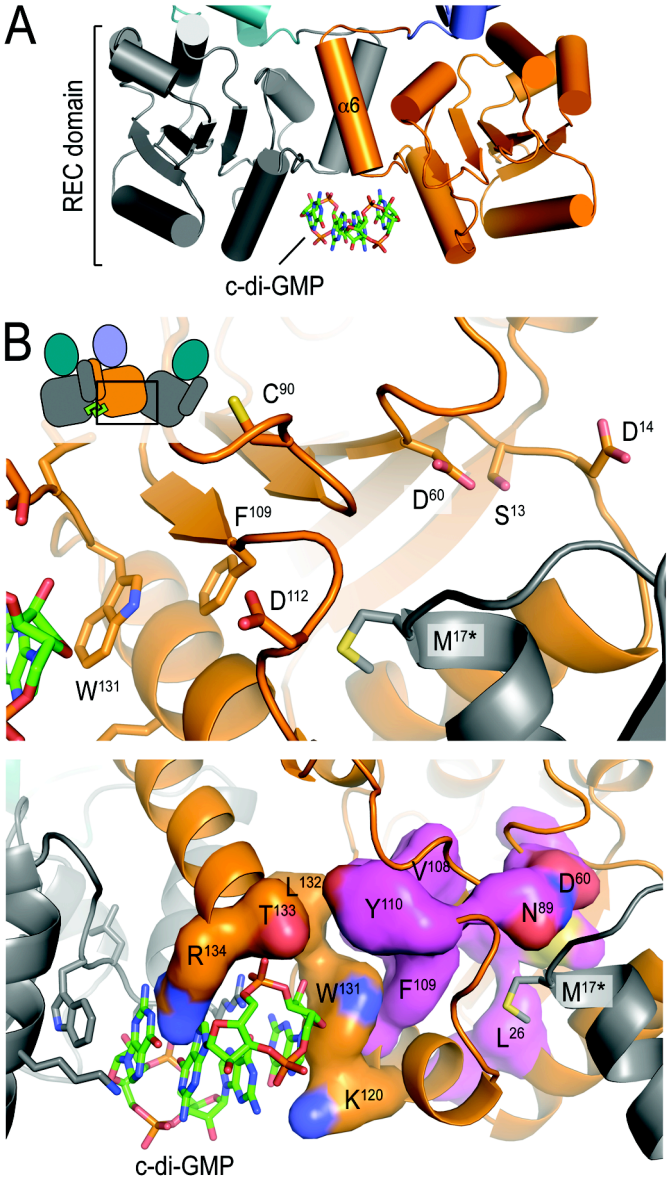

Figure S11: Krasteva *et al.*

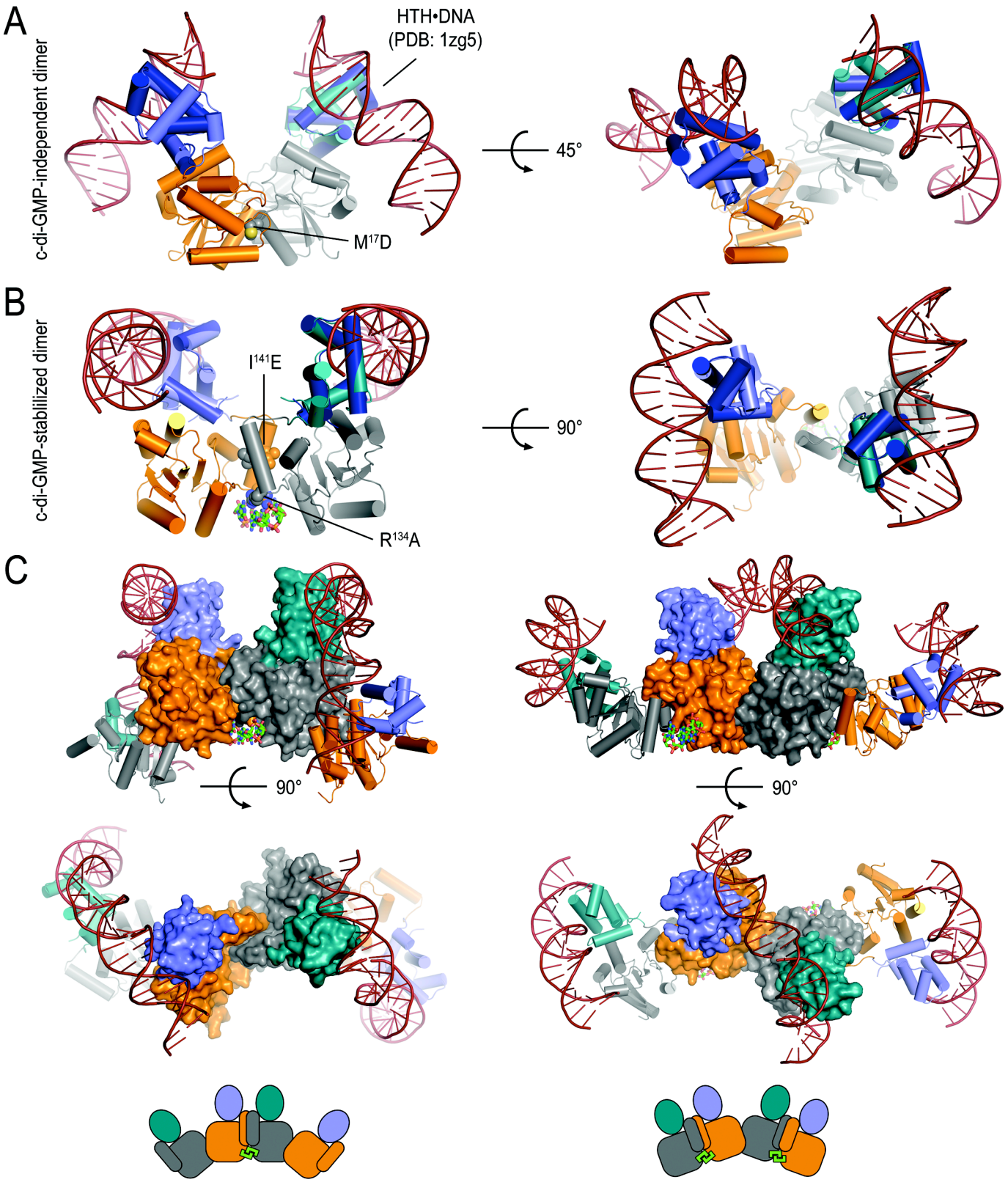

Figure S12: Krasteva *et al.*

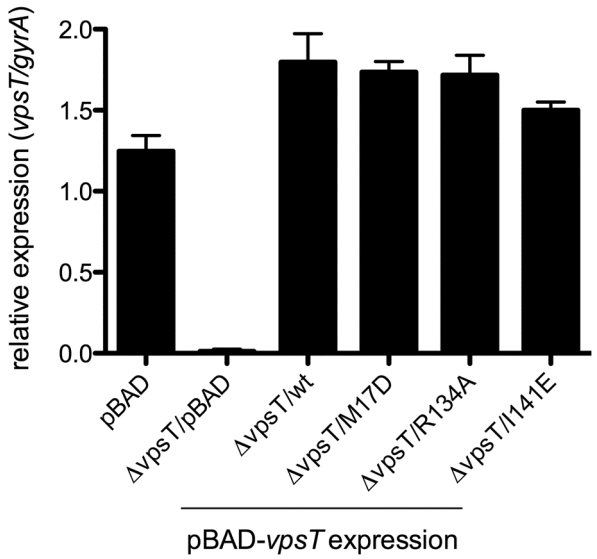

Figure S13: Krasteva *et al.*